

Thermal Tensor Network Approach for Spin-Lattice Relaxation in Quantum Magnets

Ning Xi,^{1,2,*} Yuan Gao,^{3,1,*} Chengchen Li,⁴ Shuang Liang,^{5,6} Rong Yu,^{4,7,†} Xiaoqun Wang,^{2,‡} and Wei Li^{1,3,§}

¹CAS Key Laboratory of Theoretical Physics, Institute of Theoretical Physics, Chinese Academy of Sciences, Beijing 100190, China

²School of Physics, Zhejiang University, Hangzhou, 310058, China

³Peng Huanwu Collaborative Center for Research and Education, School of Physics, Beihang University, Beijing 100191, China

⁴Department of Physics and Beijing Key Laboratory of Opto-electronic Functional Materials and Micro-nano Devices, Renmin University of China, Beijing 100872, China

⁵Institute of Physics, Chinese Academy of Sciences, Beijing 100190, China

⁶Yangtze River Delta Physics Research Center, Liyang, Jiangsu 213300, China

⁷Key Laboratory of Quantum State Construction and Manipulation (Ministry of Education), Renmin University of China, Beijing, 100872, China

(Dated: March 21, 2024)

Low-dimensional quantum magnets, particularly those with strong spin frustration, are characterized by their notable spin fluctuations. Nuclear magnetic resonance (NMR) serves as a sensitive probe of low-energy fluctuations that offers valuable insight into rich magnetic phases and emergent phenomena in quantum magnets. Although experimentally accessible, the numerical simulation of NMR relaxation rates, specifically the spin-lattice relaxation rate $1/T_1$, remains a significant challenge. Analytical continuation based on Monte Carlo calculations are hampered by the notorious negative sign for frustrated systems, and the real-time simulations incur significant costs to capture low-energy fluctuations. Here we propose computing the relaxation rate using thermal tensor networks (TTNs), which provides a streamlined approach by calculating its imaginary-time proxy. We showcase the accuracy and versatility of our methodology by applying it to one-dimensional spin chains and two-dimensional lattices, where we find that the critical exponents η and $z\nu$ can be extracted from the low-temperature scalings of the simulated $1/T_1$ near quantum critical points. Our results also provide insights into the low-dimensional and frustrated magnetic materials, elucidating universal scaling behaviors in the Ising chain compound CoNb_2O_6 and revealing the renormalized classical behaviors in the triangular-lattice antiferromagnet $\text{Ba}_8\text{CoNb}_6\text{O}_{24}$. We apply the approach to effective model of the family of frustrated magnets AYbCh_2 ($A = \text{Na, K, Cs, and Ch} = \text{O, S, Se}$), and find dramatic changes from spin ordered to the proposed quantum spin liquid (QSL) phase. Overall, with high reliability and accuracy, the TTN methodology offers a systematic strategy for studying the intricate dynamics observed across a broad spectrum of quantum magnets and related fields.

I. INTRODUCTION

Frustrated quantum magnets offer an ideal material platform for investigating rich many-body phases and phenomena. They are characterized by unconventional magnetically ordering such as spin supersolidity [1] and fractional magnetization plateau state [2], and disordered spin states like the quantum spin liquid (QSL) that remain strongly fluctuating even down to zero temperature. The QSL does not show any symmetry breaking, yet has intrinsic topological order and hosts fractional excitations, beyond the Landau theory of phases of matter [3–6].

The studies of frustrated magnets demand an integration of advanced many-body approaches with experimental methodologies, in particular spectroscopic measurements at very low temperature. Amongst various dynamical measurements, nuclear magnetic resonance (NMR) constitutes an exceptionally sensitive probe of low-energy excitations. The NMR relaxation rates, including the spin-lattice relaxation rate $1/T_1$ and the spin-echo decay rate T_{2G} , offer the advantage of capturing

contributions of very low energy excitations and from various momenta across the Brillouin zone (BZ).

NMR has been widely used in the investigations of low-dimensional quantum magnets [7–18]. In particular, it serves as a very powerful and rather unique technique in the studies of highly frustrated QSL candidate materials. For example, in spin-chain compounds the observed scalings of relaxation rates $1/T_1$ reveal the Tomonaga-Luttinger liquid (TLL) behaviors [7, 8] and Ising quantum criticality [9, 13–15]. For 2D quantum magnets, the temperature dependence of $1/T_1$ has also been employed to detect the Kosterlitz-Thouless phase in triangular-lattice quantum antiferromagnet TmMgGaO_4 [16, 19], possible quantum spin liquid in the Kitaev candidate $\alpha\text{-RuCl}_3$ [17], and the proximate deconfined quantum critical point (QCP) in the Shastry-Sutherland magnet $\text{SrCu}_2(\text{BO}_3)_2$ [18, 20], among others.

From the theoretical side, except for few exactly solvable systems [8, 9, 21, 22], calculations of the spin-lattice relaxation rate $1/T_1$ with precision pose significant challenges. Specifically, by taking the strictly local hyperfine form factor [10, 11], the spin-lattice relaxation rate can be evaluated as

$$1/T_1 \propto \mathcal{S}(\omega = 0) \simeq \lim_{\omega \rightarrow 0} T \sum_{\mathbf{q}} \sum_{\alpha=x,y,z} \chi''_{\alpha\alpha}(\mathbf{q}, \omega)/\omega, \quad (1)$$

where $\chi''_{\alpha\alpha}(\mathbf{q}, \omega)$ is the imaginary part of the dynamical sus-

* These authors contributed equally to this work.

† rong.yu@ruc.edu.cn

‡ xiaoqunwang@zju.edu.cn

§ w.li@itp.ac.cn

ceptibility of spin component α and at momentum \mathbf{q} , with $S(\omega = 0)$ the static spin structure factor. To compute the spin-lattice relaxation [23–26], one first needs to prepare the low-temperature equilibrium state as an initial step for dynamic simulations. Following this, real-time evolution should be performed to long time scales, to provide sufficient energy resolution into the low-energy spectroscopy. Both steps present significant challenges in many-body calculations.

Alternatively, in quantum Monte Carlo (QMC) calculations there have been attempts to calculate $1/T_1$ from imaginary-time correlation functions by using numerical analytical continuation [10–12, 27, 28]. A large collection of algorithms have been developed to deal with the somewhat ill-posed analytical continuation problem, including maximal entropy [12, 29], stochastic analytic continuation [30], stochastic pole expansion [31, 32], and Nevanlinna analytical continuation [32, 33], etc. However, these approaches necessitate the careful selection of a specific scheme and the meticulous adjustment of hyperparameters, to capture the essential features inherent in the spectral function. One way to avoid numerical analytical continuation is resorting to the imaginary-time proxy (ITP). In early years ITP has been exploited to simulate the attractive electron Hubbard model [34], and recently also to quasi-1D spin chain systems [27, 35], within QMC calculations. However, this approach were hindered when applied to the frustrated magnets and fermion lattices away from half filling, by the notorious sign problem in QMC.

Thermal tensor networks (TTN) and their renormalization group methods provide an efficient and accurate approach for simulating the quantum lattice systems down to low temperature [36–48]. In particular, the matrix product operator (MPO) based approaches [see Fig. 1(a)], including the linearized tensor renormalization group (TRG) [41, 45], exponential TRG [44, 46], and the tangent-space TRG [48] have been developed to simulate large-scale quantum spin systems [49, 50] and the doped Hubbard-type models [48, 51, 52] down to low temperatures. Recently, they have been applied to study the TLLs in 1D spin chains [53, 54], triangular-lattice antiferromagnets [1, 16, 55–57], and the honeycomb Kitaev magnets [58–61], among others.

In this study, we demonstrate that the cutting-edge TTN methodology serves as a potent tool for assessing the spin-lattice relaxation rates, specifically $1/T_1$. This is achieved by calculating the ITPs at zero frequency: first-order proxy $\mathcal{S}_1(\omega = 0)$ or second-order $\mathcal{S}_2(\omega = 0)$, as defined in the subsequent analysis. Note that the TTN is free of sign problem, and this approach is thus capable of studying $1/T_1$ in the frustrated quantum magnets. With this approach, we reveal the TLL scalings of the 1D XXZ Heisenberg antiferromagnetic chain and the quantum critical behavior of the 2D transverse-field Ising model by accurately extracting η and $z\nu$ critical exponents from $\mathcal{S}_{1,2}(\omega = 0)$. Moreover, we extract the site- and momentum-resolved spin excitation gaps of spin-1 Heisenberg chain, providing an accurate estimate of the renowned Haldane gap. For the square-lattice Heisenberg model, the temperature scale of renormalized classical regime is obtained.

We apply this approach also to analyze the NMR measure-

ments on realistic quantum magnets, including the Ising chain compound CoNbO_6 and triangular lattice Heisenberg antiferromagnet $\text{Ba}_8\text{CoNb}_6\text{O}_{24}$. For the Ising chain case, inspired by the model calculation results we perfectly collapse the experimental data and accurately determine the critical fields and exponents $\eta, z\nu$ in CoNbO_6 . With triangular-lattice Heisenberg model calculations, we obtain similar behaviors in $1/T_1$ as observed in the compound $\text{Ba}_8\text{CoNb}_6\text{O}_{24}$, where two temperature scales can be identified. The triangular-lattice QSL candidate AYbCh_2 family has raised great interest recently, whose coupling can be tuned by substituting the alkali elements $A=\text{Na, K, Cs}$, and $\text{Ch}=\text{O, S, Se}$ [62–65]. Our simulated $1/T_1$ results of the effective J_1 - J_2 triangular-lattice model pave the way for the NMR probe of possible QSL in this highly frustrated material family.

The rest of the paper is organized as follows. In Sec. II we introduce the TTN approach and low-dimensional lattice models used in the present work. Section III presents our main results of 1D and 2D lattice models, with a focus on the universal scalings in $1/T_1$ of spin-1/2 Heisenberg chain and estimate of spin gap in spin-1 Haldane chain. The square-lattice transverse-field Ising and Heisenberg models are also studied. In Sec. IV we compare our model calculations with NMR measurements on realistic compounds, including the spin-chain material CoNb_2O_6 and the triangular-lattice antiferromagnet $\text{Ba}_8\text{CoSb}_6\text{O}_{24}$. Section V is devoted to the summary and outlook.

II. MODELS AND METHODS

A. Quantum spin models

In this work, we consider two types of spin models defined on several 1D and 2D lattices, which include the Heisenberg antiferromagnet (HAF) and transverse-field Ising (TFI) models. The Hamiltonian of spin- S HAF model with XXZ anisotropy reads

$$H_{\text{XXZ}} = \sum_{\langle i,j \rangle} J_{xy}(S_i^x S_j^x + S_i^y S_j^y) + J_z S_i^z S_j^z, \quad (2)$$

where J_{xy} (J_z) represents the coupling between nearest neighboring (NN) sites within xy -plane (along z -axis). In the present study we take $J_{xy} \equiv 1$ as the energy scale, and the isotropic HAF model corresponds to $J_z = J_{xy} = 1$. We consider the $S = 1/2$ and $S = 1$ HAF chains in 1D, as well as the $S = 1/2$ HAF model on the square and triangular lattices in 2D.

The Hamiltonian of TFI models on both 1D chain and 2D square lattice can be written as

$$H_{\text{Ising}} = -J \sum_{\langle i,j \rangle} S_i^z S_j^z - h \sum_i S_i^x, \quad (3)$$

where $J \equiv 1$ is the energy scale of the ferromagnetic TFI model, and h is the transverse field tuning quantum fluctuations. The critical fields in the two models are $h_c = 0.5$ (for

the 1D chain) and $h_c \simeq 1.522$ [66] (for the square lattice), which separate the spin ordered and paramagnetic disordered phases.

B. Thermal tensor network renormalization

In the calculations below, we employ the linearized TRG (LTRG) [41] for 1D and tangent-space TRG (tanTRG) [48] for 2D lattices to obtain the equilibrium density operator $\rho(\beta)$ and estimate the imaginary-time proxies $\mathcal{S}_{1,2}$. In both approaches, we perform imaginary-time evolutions of the density matrix $\rho(\beta)$ following the equation $d\rho/d\beta = -H\rho$, where β is the inverse temperature, and the initial state $\rho(\beta = 0) \equiv I$. For 1D HAF and TFI spin chains, the finite- T density matrices $\rho(\beta)$ has an efficient matrix product operator (MPO) representation as shown in Fig. 1(a), which can be obtained by LTRG [41, 45] (see also Appendix A 1). In practice, we exploit 6th-order Trotter-Suzuki decomposition [67] so that the discretization error is sufficiently small in our calculations. In the LTRG process, bond dimension of the MPO $\rho(\beta)$ generically increases as the inverse temperature β increases, and we retain bond dimension up to $\chi = 600$ that produces fully converged data in 1D systems.

For the 2D HAF and TFI models, we exploit the tanTRG approach firstly invented to deal with 2D many-electron problems [48, 68] and here also applicable to quantum spin models [20]. To tackle the finite-size 2D lattices, we map them into quasi-1D system with long-range interactions, and represent the density matrix $\rho(\beta)$ also as an MPO [c.f., Fig. 1(c)]. Using techniques from the time-dependent variational principle [69, 70], we integrate the evolution equation restricted within the MPO manifold of a given bond dimension. In practice, cylindrical geometries are considered with widths up to $W = 12$ for the square-lattice TFI, $W = 8$ for the square-lattice HAF, and $W = 6$ for the triangular-lattice HAF models. The retained bond dimension is up to $\chi^* = 4000$ multiplets (equivalently $\chi \simeq 16,000$ individual states) for the 2D models.

C. Imaginary-time proxies $\mathcal{S}_{1,2}(0)$ for $1/T_1$

With the density matrix $\rho(\beta)$ obtained, we further compute the imaginary-time spin correlators

$$\langle S_i^\alpha(\tau) S_j^\alpha \rangle = \frac{1}{\mathcal{Z}(\beta)} \text{Tr}[e^{(-\beta+\tau)\hat{H}} S_i^\alpha e^{(-\tau)\hat{H}} S_j^\alpha], \quad (4)$$

where $\mathcal{Z}(\beta) = \text{Tr}[\rho(\beta)]$ is the partition function. The spin correlator is related to the imaginary dynamical susceptibility $\chi''_{\alpha\alpha}(\mathbf{q}, \omega)$ via

$$\langle S_{-q}^\alpha(\tau) S_q^\alpha(0) \rangle = \frac{1}{2\pi} \int d\omega \frac{e^{-\omega\tau}}{1 - e^{-\omega\beta}} \chi''_{\alpha\alpha}(\mathbf{q}, \omega). \quad (5)$$

One can calculate $1/T_1^{\alpha\alpha}$ by first extracting $\chi''_{\alpha\alpha}(\mathbf{q}, \omega)$ from Eq. (5) by using numerical analytical continuation, then plug

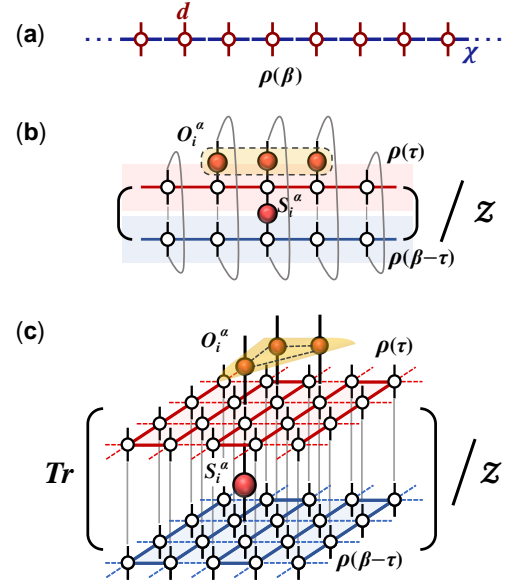


FIG. 1. (a) The MPO representation of density matrix $\rho(\beta)$ of 1D quantum spin chains. The geometric bond dimension is denoted as χ and the local Hilbert space dimension as d . The tensor network evaluation of the imaginary-time proxies $\mathcal{S}_{1,2}(\omega = 0)$ are illustrated for (b) 1D chain and (c) 2D lattice mapped into quasi-1D system. $\mathcal{Z} \equiv \text{Tr}[\rho(\beta)]$ is the partition function, and the ITPs $\mathcal{S}_1(0)$ and $\mathcal{S}_2(0)$ can be computed by tracing the bilayer tensor network with local operators S_i^α and O_i^α (see definition in the main text).

it into Eq. (1). There are a variety of specific techniques invented to effectively extract the dynamical information, each with its own advantages and limitations [10–12, 27–33].

Alternatively, here we resort to an efficient and convenient proxy that extracts the low-energy dynamics from imaginary-time correlator in the large- β limit. Taking $\tau = \beta/2$ in Eq. (5), we arrive at

$$\langle S_{-q}^\alpha(\beta/2) S_q^\alpha(0) \rangle = \frac{1}{2\pi} \int d\omega \frac{\chi''_{\alpha\alpha}(\mathbf{q}, \omega)}{2 \sinh(\beta\omega/2)}. \quad (6)$$

Assuming $\chi''_{\alpha\alpha}(\mathbf{q}, \omega)$ is analytic at $\omega = 0$, we conduct Taylor expansion

$$\begin{aligned} \chi''_{\alpha\alpha}(\mathbf{q}, \omega) &= \omega \sum_{n=0}^{\infty} \frac{\omega^{2n}}{(2n+1)!} \left. \frac{d^n \chi''_{\alpha\alpha}(\mathbf{q}, \omega)}{d\omega^n} \right|_{\omega=0} \\ &= \omega \sum_n f_n^{\alpha\alpha}(\mathbf{q}, \omega), \end{aligned} \quad (7)$$

where only odd terms in ω are allowed. Substitute the expansion in Eq. (7) into Eq. (6), we retain only the leading order in ω

$$\begin{aligned} \langle S_{-q}^\alpha(\beta/2) S_q^\alpha(0) \rangle &\approx \frac{1}{4\pi} \left[\left(\frac{2}{\beta} \right)^2 f_0^{\alpha\alpha}(\mathbf{q}, 0) \int_0^\infty d\tilde{\omega} \frac{\tilde{\omega}}{\sinh(\tilde{\omega})} \right] \\ &\stackrel{\beta \rightarrow \infty}{\approx} \frac{\pi}{2\beta^2} f_0^{\alpha\alpha}(\mathbf{q}, 0), \end{aligned} \quad (8)$$

where the dimensionless parameter $\tilde{\omega} = \beta\omega/2$.

On the other hand, by substituting the expansion of $\chi''(\mathbf{q}, \omega)$ into Eq. (1), we retain the lead order term and obtain

$$\mathcal{S}(\omega = 0) \simeq \frac{1}{\beta} \sum_{\mathbf{q}} \sum_{\alpha} f_0^{\alpha\alpha}(\mathbf{q}, 0). \quad (9)$$

By comparing Eq. (8) with Eq. (9), we arrive at

$$\mathcal{S}_1(\omega = 0) \simeq \beta \sum_{\mathbf{q}} \sum_{\alpha} \langle S_{-\mathbf{q}}^{\alpha}(\beta/2) S_{\mathbf{q}}^{\alpha} \rangle \quad (10)$$

where $\mathcal{S}_1(\omega = 0)$ is introduced as a proxy for $1/T_1$ (up to a constant factor) in the large β limit. Equation (10) shows that the dynamical spin structure, and also the spin-lattice relaxation rate, can be obtained conveniently via the imaginary-time correlation.

Below we compute $\mathcal{S}_1(0)$ for various systems at low temperature $T \lesssim J$. For gapped systems, it is obvious that $S_1^{\alpha\alpha}(\mathbf{q}, \omega = 0) \equiv \beta \langle S_{-\mathbf{q}}^{\alpha}(\beta/2) S_{\mathbf{q}}^{\alpha} \rangle$ decay exponentially following $\exp[-\Delta_S(\mathbf{q})/T]$, with $T = 2/\beta$ and $\Delta_S(\mathbf{q})$ the spin excitation gap at momentum \mathbf{q} . One remark is that Eq. (7) relies on the assumption that $\chi''(\mathbf{q}, \omega)$ is analytical at $\omega = 0$. In certain gapped systems, $\chi''(\mathbf{q}, \omega)$ may have a pole and hence become singular at $\omega = 0$. For those systems, we can single out the pole, calculate its contribution to $1/T_1$ separately, and treat the regular part as described above.

Along a similar line, we can define the second-order proxy, $\mathcal{S}_2(0)$ to $1/T_1$, by taking derivatives of the correlator $\langle S_{-\mathbf{q}}^{\alpha}(\tau) S_{\mathbf{q}}^{\alpha} \rangle$ with respect to the imaginary time τ in Eq. (5), namely,

$$\partial_{\tau}^2 \langle S_{-\mathbf{q}}^{\alpha}(\tau) S_{\mathbf{q}}^{\alpha}(0) \rangle = \frac{1}{2\pi} \int d\omega \frac{\omega^2 e^{-\omega\tau}}{1 - e^{-\omega\beta}} \chi''_{\alpha\alpha}(\mathbf{q}, \omega). \quad (11)$$

Once again we take $\tau = \beta/2$, insert the Taylor expansion of $\chi''_{\alpha\alpha}(\mathbf{q}, \omega)$ in Eq. (7), and retain the leading order in ω , i.e.,

$$\partial_{\tau}^2 \langle S_{-\mathbf{q}}^{\alpha}(\tau) S_{\mathbf{q}}^{\alpha} \rangle |_{\tau=\beta/2} \stackrel{\beta \rightarrow \infty}{\approx} \frac{\pi^3}{\beta^4} f_0(\mathbf{q}, 0). \quad (12)$$

With Eq. (9) we arrive at the expression of the second-order proxy,

$$\mathcal{S}_2(\omega = 0) \equiv \beta^3 \sum_{\mathbf{q}} \sum_{\alpha} \partial_{\tau}^2 \langle S_{-\mathbf{q}}^{\alpha}(\tau) S_{\mathbf{q}}^{\alpha} \rangle |_{\tau=\beta/2} \sim 1/T_1. \quad (13)$$

In practice, the second-order derivative can be evaluated following

$$\begin{aligned} & \partial_{\tau}^2 \langle S_j^{\alpha}(\tau) S_j^{\alpha} \rangle |_{\tau=\tau_0} \\ &= \frac{1}{\mathcal{Z}} \text{Tr} (e^{(-\beta+\tau_0)H} [H, [H, S_j^{\alpha}]] e^{(-\tau_0)H} S_j^{\alpha}) \\ &= \langle O_j^{\alpha}(\tau_0) S_j^{\alpha} \rangle, \end{aligned} \quad (14)$$

where $O_j^{\alpha} = [H, [H, S_j^{\alpha}]]$ is the commutator, and thus we have $\mathcal{S}_2^{\alpha\alpha}(\omega = 0) = \beta^3 \sum_j \langle O_j^{\alpha}(\beta/2) S_j^{\alpha} \rangle$.

As shown in Figs. 1(b,c), $\mathcal{S}_1(0)$ and $\mathcal{S}_2(0)$ can be evaluated

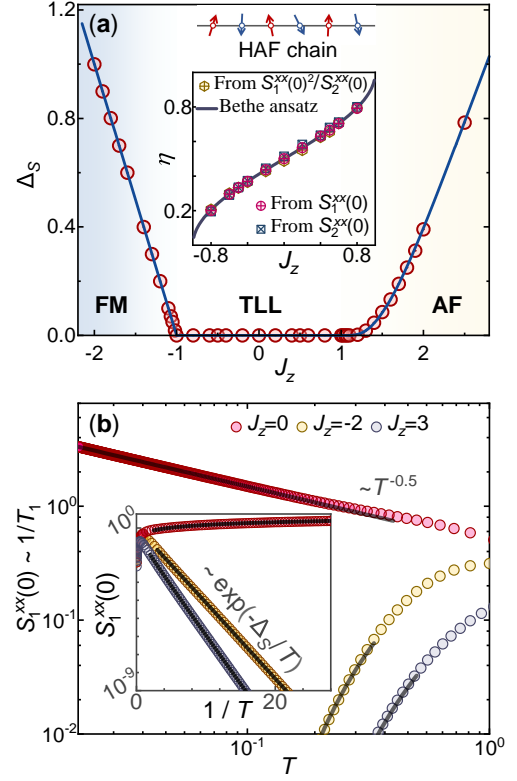


FIG. 2. (a) shows the results of spin-1/2 HAF chain with varying $-2 \leq J_z \leq 3$ and fixed $J_{xy} \equiv 1$. In both the gapped FM and AF phases, the spin gaps Δ_S are calculated from the exponential decay of $S_1^{xx}(0)$ at low temperatures. The inset demonstrates the exponent η fitted in the TLL phase using three distinct proxies (see Appendix B), all of which align perfectly with the analytical results (purple line) from Bethe ansatz. This validates the precision and reliability of our method. (b) The calculated $S_1^{xx}(0) \sim 1/T_1$ data and their low- T scalings in the spin-1/2 HAF chain with $J_z = 0, -2, 3$. In the FM ($J_z = -2$) and AF ($J_z = 3$) phases, $S_1^{xx}(0)$ decays exponentially as further elaborated in the inset; for the XY case ($J_z = 0$), $S_1^{xx}(0)$ manifests an algebraic scaling $T^{\eta-1}$ with the anomalous dimension $\eta = 1/2$.

as imaginary-time correlations. They are obtained by contracting the two MPOs, each representing the density matrix $\rho(\beta/2)$, with the local operators S_i^{α} and O_i^{α} defined above. The ITPs $\mathcal{S}_{1(2)}(0)$ offer an expedient and fast way to estimate the finite-temperature and low-frequency dynamics, achieving a computational efficiency akin to traditional thermodynamic calculations performed within TTN framework.

III. RESULTS

A. Spin-lattice relaxation in the TLL phase of spin chains

We consider the prototypical spin-1/2 HAF chain with an XXZ anisotropy [c.f., Eq. (2)], and estimate the spin-lattice relaxation rate $1/T_1$ by computing the proxies $\mathcal{S}_{1(2)}(0)$. As the anisotropy J_z varies from -2 to 3, the system changes from

the easy-axis ferromagnetic (FM), through the gapless TLL phase, to the Ising AF phases.

In Fig. 2(a), we show the results of spin excitation gaps Δ_S extracted from $S_1^{xx}(0)$, where the gap scales linearly versus $|J_z|$, namely, $\Delta_S = -J_z - 1$ in the FM phase; while it follows an exponential behavior, i.e., $\Delta_S \sim \exp(-\xi/\sqrt{|J_z - 1|})$ in the AF phase [71] (ξ is a constant, see Appendix B), indicating the occurrence of a Berezinskii-Kosterlitz-Thouless (BKT) transition at $J_z = 1$. In Fig. 2(b), we show the details of temperature scalings in $S_1^{xx}(0)$, which decay exponentially as $\exp(-\Delta_S/T)$ in both the easy-axis FM and AF phases with $|J_z| > 1$.

In the intermediate TLL phase with $|J_z| < 1$, we find algebraic behaviors $S_1^{xx}(0) \sim T^{(\eta+d-2)/z}$ [18, 72], where d is the spatial dimension, z is the dynamical exponent, and η represents the anomalous dimension that relates to the Luttinger parameter via $K = 1/4\eta$. In particular, in Fig. 2(b) we find $S_1^{xx}(0) \sim T^{-1/2}$ in the $J_z = 0$ case, consistent with the expectation of $z = 1$ and $\eta = 1/2$ for the XY chain. Tuning the coupling away from $J_z = 0$, we estimate the exponents η from the scalings of $S_{1,2}^{xx}(0)$, and the ratio $S_2^{xx}(0)^2/S_1^{xx}(0)$ from each parameter J_z (see more details in Appendix B). The results are collected in the inset of Fig. 2(a), which agree excellently with the analytical results from Bethe ansatz [73].

B. Topological edge mode and the spin gap in the spin-1 Haldane chain

Initially proposed theoretically [75, 76] and subsequently verified via high-precision DMRG calculations [74, 77], the spin-1 HAF chain described by Eq. (2) with $J_{xy} = J_z = 1$ exhibits a gapped Haldane phase. This phase has been proposed to host the symmetry-protected topological order [78], and supports free spin-1/2 edge states that reside at both open boundaries of the spin chain. The topological edge mode exponential decays as moving into the bulk of the system [74]. In Fig. 3 we show the simulated $S_1(0) \sim 1/T_1$ of the $S = 1$ HAF chain. The spatial and momentum distribution of $S_1(0)$ can be obtained, from which the Haldane gap and topological edge modes are extracted.

To reveal the edge modes, we introduce the site-resolved relaxation rate $S_1(i, \omega = 0) = \beta \langle S_i(\beta/2) S_i(0) \rangle$, where i label the site in the spin chain of length L . In Fig. 4(a) we show results at different site i of the spin-1 HAF chain (with open boundary conditions), and find the spins become ‘‘asymptotically free’’ as approaching both ends of the chain. This is revealed by the scaling $S_1(i \ll L/2, \omega = 0)$ at low temperature, which diverges as $1/T$ and reflects the existence of zero mode at the boundary. On the other hand, as i moves into the bulk, the calculated $S_1(i \approx L/2, \omega = 0)$ join the exponential decaying behavior as in an infinite chain. The fitted spin gap from the exponential scaling is $\Delta_S \simeq 0.410(1)$ [c.f., Fig. 3(a)], which is in excellent agreement with the DMRG results of the Haldane gap [74].

The momentum dependence of the spin excitation gap $\Delta_S(q)$ can also be extracted by fitting the exponential scaling $S_1(q, \omega = 0) \sim 1/T \exp[-\Delta_S(q)/T]$, which are shown

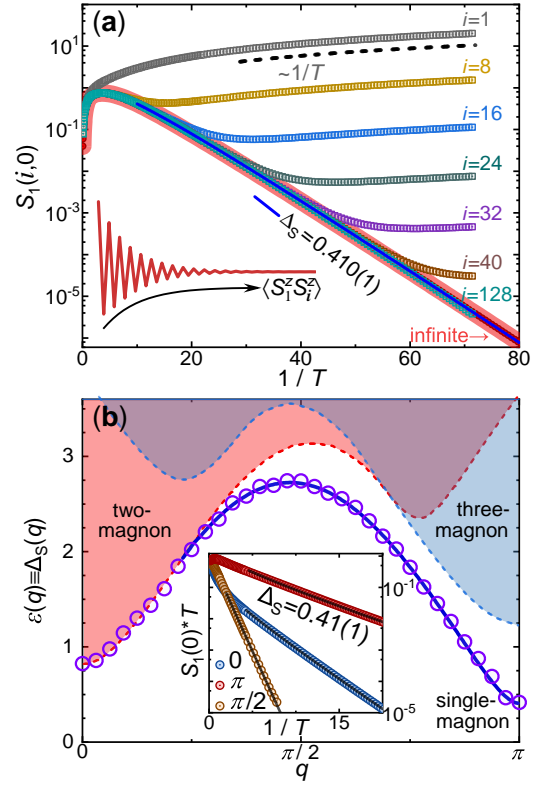


FIG. 3. (a) The site-resolved results $S_1(i, 0)$ measured at various sites i of the $L = 256$ chain, plotted with the results obtained directly in the thermodynamic limit (red squares labeled as ‘‘infinite’’). The $1/T$ scaling for i near the ends of the chain reflects the zero edge modes. In the bulk of the chain it decays exponentially with (inverse) temperature, from which the Haldane gap $\Delta_S \simeq 0.410(1)$ can be accurately fitted. (b) The momentum-resolved spin gap $\Delta_S(q)$ (open purple circle) for the spin-1 HAF chain estimated from the exponential decay of $T S_1(q, \omega = 0) \sim \exp[-\Delta_S(q)/T]$ (see the inset). The Haldane gap can also be estimated at momentum $q = \pi$, where $\Delta_S(\pi) \simeq 0.41(1)$. The single-magnon dispersion (blue solid line), two-magnon continua (red shaded range), and three-magnon continua (blue shaded range) are adapted from Ref. [74].

in Fig. 4(b). For $q \gtrsim \pi/4$, $\Delta_S(q)$ reproduces the single-magnon dispersion [74], while for $q \lesssim \pi/4$ $\Delta_S(q)$ follows the lower boundary of the two-magnon continuum. The two-magnon bound state has lower energy than that of the single-magnon excitation, and $S_1(0)$ always captures the lowest excitation gap of the system.

C. Universal scalings near the (2+1)D Ising QCP

Below we show that our approach can be used to study the universal scalings near the QCP in 2D lattice models. In Fig. 4 we exploit state-of-the-art tanTRG approach [48] to simulate the square-lattice TFI model [c.f., Eq. (3)] on cylinder geometries with widths up to $W = 12$ [c.f., inset in Fig. 4(a)], and study the scaling behaviors of $1/T_1$ near the Ising QCP. The transverse field introduces quantum fluctuations that melt the magnetic order at $h_c \simeq 1.52$ [66].

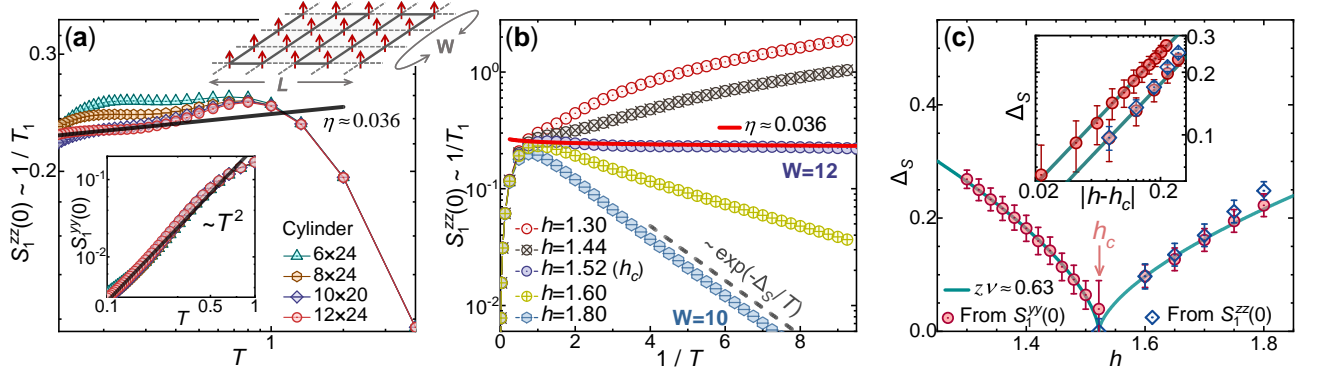


FIG. 4. (a) Simulations of spin-lattice relaxation rate in the square-lattice TFI model defined on cylinders (see upper right inset) with different system widths up to $W = 12$. The low-temperature scaling of $1/T_1 \sim S_1^{zz}(0)$ at the QCP follow the scaling T^η (with $\eta \simeq 0.036$) as indicated by the solid line. $S_1^{yy}(0)$ is also computed and found to scale as T^2 (bottom left inset). (b) The behaviors of $S_1(0)$ for two gapped phases, ordered for $h < h_c \simeq 1.52$ and quantum disordered for $h > h_c$, are in sharp contrast to that at the QCP $h = h_c$. We perform the calculations on 10×20 cylinder for gapped phase and show the results at QCP on the largest system size 12×24 . (c) Red circles represent estimated spin gaps Δ_S from $S_1^{yy}(0)$ (for both $h < h_c$ and $h > h_c$) and the blue diamonds are from $S_1^{zz}(0)$ for $h > h_c$. We find $\Delta_S \propto |h - h_c|^{z\nu}$ near the QCP, with exponent $z\nu \simeq 0.63$ as indicated by the blue lines. The inset presents a log-log plot of the data, which more clearly illustrates this universal algebraic scaling.

In Fig. 4(a), we find that as system size increases $S_1^{zz}(0)$ gradually falls into the universal scaling $S_1^{zz}(0) \sim T^\eta$ with $\eta \simeq 0.036$, consistent with the (2+1)D Ising universality class. We also find that $1/T_1$ exhibits strong anisotropic behaviors, and show $S_1^{yy}(0)$ in the lower left inset of Fig. 4(a), which reveals a different algebraic scaling $S_1^{yy}(0) \sim T^2$. In Fig. 4(b), the results of $S_1^{zz}(0)$ are shown in both gapped phases, where we find it decays exponentially for the ordered phase with $h < h_c$ while diverges in the paramagnetic phase for $h > h_c$, in sharp contrast to the scaling behaviors right at QCP.

Based on the $S_1(0)$ data obtained in the two gapped phases, we further extract the spin gap Δ_S from the exponential decaying behaviors [c.f., Appendix B]. The so-determined spin gaps are collected and shown in Fig. 4(c), and we find the results fall into an algebraic scaling $\Delta_S \propto |h - h_c|^{z\nu}$ near the Ising QCP, with the fitted exponent $z\nu \simeq 0.63$ again consistent with the (2+1)D Ising universality class.

D. Renormalized classical behaviors on the square lattice

According to the Mermin-Wagner theorem, the square-lattice HAF (SLHAF) system remains disordered at all finite temperatures. However, a crossover occurs at certain characteristic temperature scale T_m , below which the system exhibits the renormalized classical (RC) behaviors. Within the RC regime, the correlation length and spin-lattice relaxation $1/T_1$ exhibit exponential divergence as temperature lowers [11, 79].

In Fig. 5, we simulate such RC behavior through $S_1(0)$ with TTN and QMC calculations, where the former is obtained on the 8×16 cylinder and the latter on a larger, 16×16 lattice with periodic boundary conditions (PBCs). The excellent agreement reveals that $S_1(0)$ results are stable on different lattice geometries, and both results increase rapidly below about $T_m \sim 0.55J$. As shown in the inset of Fig. 5(a), the simulated

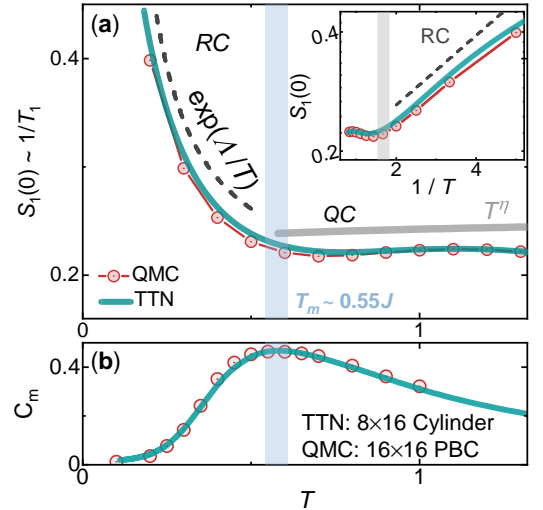


FIG. 5. (a) The calculated $S_1(0)$ for the SLHAF model. Results are shown for a width-8 cylinder (length $L = 16$) using TTN, represented by the cyan line, and a 16×16 square lattice (with both PBC) using QMC, denoted by the red solid point. (b) shows the specific heat data calculated by TTN (cyan line) and QMC (red markers). exponential diverging behavior $1/T_1 \sim \exp(\Lambda/T)$ in the RC regime. The dashed and solid gray lines are guides to eyes, illustrating the exponential divergence in the RC region characterized by $\Lambda \simeq 0.2$ and the quantum-critical (QC) behavior associated with the 3D Heisenberg exponent of $\eta \simeq 0.035$, respectively. The shaded area denotes the crossover temperature scales $T_m \simeq 0.55J$.

$S_1(0)$ follows an exponential diverging scaling $\exp(\Lambda/T)$ in the RC regime, below a possible QC regime at intermediate temperature.

In Fig. 5(b), we present the results of the specific heat C_m obtained from TTN and QMC calculations. Despite the differences in their respective geometries (8×16 cylinder vs.

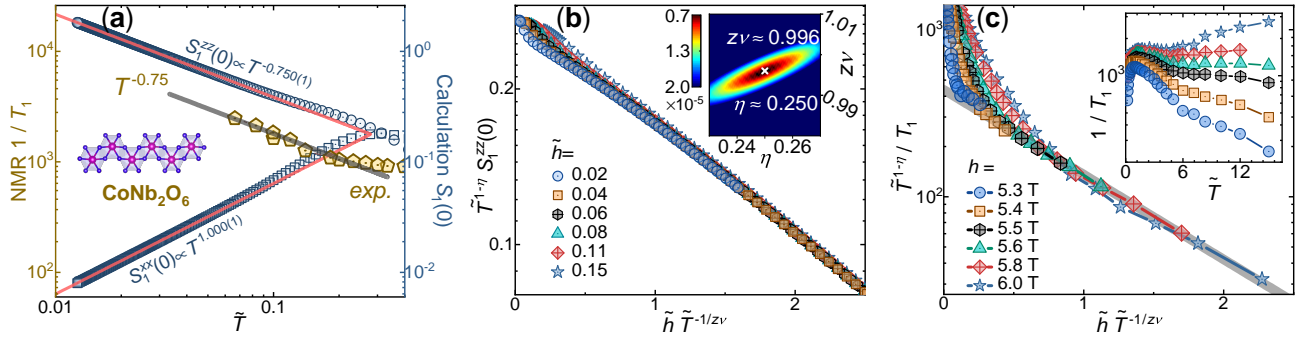


FIG. 6. (a) shows the calculated $S_1^{x,x,z,z}$ of the TFI chain near QCP ($\tilde{h} = 0$) and makes a comparison to the experimental $1/T_1$ data. The dimensionless parameters are defined as $\tilde{h} = (h - h_c)/h_c$ and $\tilde{T} = T/J$, with $J \simeq 30$ K and $h_c \simeq 5.2$ T for CoNb_2O_6 . The navy markers (\odot for $S_1^{x,x}$ and \square for $S_1^{z,z}$) are from the model calculations, and the brown pentagons are NMR measurements on CoNb_2O_6 [13]. $S_1^{z,z}(0) \propto T^{-0.75}$ dominates the scaling behaviors at low temperature and is in excellent agreement with NMR experiments. (b) reveals the universal scaling by collapsing the calculated $S_1^{z,z}(0)$ data near the QCP, from which we find the critical exponents are in excellent agreement with (1+1)D Ising universality class. The inset shows the contour map of the root mean square error (RMSE) in the $z\nu$ - η parameter space, where the minimum is located at $z\nu \simeq 0.996$ and $\eta \simeq 0.250$. Following this line, we collapse the experimental $1/T_1$ data with the critical exponents of (1+1)D Ising universality class ($z\nu = 1$, $\eta = 1/4$) in panel (c). The original experimental data adapted from Ref. [13] are shown in the inset.

16×16 torus), these results again demonstrate very good agreement. In the specific heat C_m there exhibits a rounded peak at approximately $T_m \simeq 0.55J$, which, together with the rapid increasing behaviors of $S_1(0)$ at lower temperature, indicates the crossover into RC regime.

IV. COMPARISONS TO EXPERIMENTAL MEASUREMENTS ON QUANTUM MAGNETS

In this section, we switch from theoretical model calculations to the domain of realistic quantum magnets. In past years, NMR measurements have been widely applied in the studies of spin dynamics in quantum magnets. However, theoretical analyses and comparisons to measured NMR data, particularly for frustrated magnets, remain relatively scarce. Below, we focus on two compounds, namely, the quasi-1D spin chain compound CoNb_2O_6 , the triangular lattice antiferromagnet $\text{Ba}_8\text{CoNb}_6\text{O}_{24}$, and J_1 - J_2 QSL candidates AReX_2 [63, 65]. With comprehensive comparisons to NMR experiments, we analyze these experimental results in the light of theoretical model calculations.

A. Universal scaling in the Ising chain CoNb_2O_6

As a prototypical quantum spin system, the TFI chain compound CoNb_2O_6 has been shown to host intriguing critical phenomena driven by transverse fields [9, 14, 15, 80–83]. Apart from the possible complex spin-spin couplings in the realistic compound [82–84], it is believed that the critical behaviors near the QCP are nevertheless well described by the (1+1)D Ising universality class, and thus can be studied through simulating the TFI chain model. Various experiments, including the low-temperature thermodynamics [85, 86], inelastic neutron scattering [80, 87], tera-

hertz spectroscopy [81, 83], and NMR [13], etc., have been conducted to study the phenomena near QCP in spin-chain compound CoNb_2O_6 . In Fig. 6, we apply our TTN approach to study the TFI chain and compare the results to NMR measurements.

In Fig. 6(a), we show the low-temperature scaling behaviors of two spin-resolved proxies $S_1^{x,x}(0)$ and $S_1^{z,z}(0)$ at $h_x^c = 0.5$. The former follows an algebraic decay with $S_1^{x,x}(0) \sim T$, while the latter diverges as $S_1^{z,z}(0) \sim T^{\eta-1}$ with $\eta \simeq 1/4$ and thus dominates the low-temperature behaviors. Therefore, our results well explain the observed $1/T_1 \sim T^{-3/4}$ scaling observed in NMR experiments [also shown in Fig. 6(a)]. Furthermore, we also calculate the $S_1^{z,z}(0)$ in the vicinity of QCP (in the $\tilde{h} > 0$ side) and find the data fall into a universal function with properly chosen parameters and exponents. In Fig. 6(b), we plot $\tilde{T} S_1^{z,z}(0) = f(\tilde{h} \tilde{T}^{-1/z\nu})$, where $\tilde{h} = (h - h_c)/h_c$ and $\tilde{T} = T/J$, with the spin coupling $J \simeq 30$ K and the critical field $h_c \simeq 5.2$ T. Through optimal data-collapsing process, represented by the minimal RMSE, we determine critical exponents $z\nu \simeq 0.996$ and $\eta \simeq 0.25$ as depicted in the inset of the contour map, in excellent agreement with the (1+1)D Ising universality class. In light of this theoretical calculation, we effectively “condense” the experimental data with the corresponding universal scaling function, as presented in Fig. 6(c).

B. NMR probe of the incipient order in $\text{Ba}_8\text{CoNb}_6\text{O}_{24}$

Regarding the 2D antiferromagnets, it has been proposed theoretically that both square and triangular lattice Heisenberg models exhibit the RC behaviors at low temperature [79, 89], with an exponential divergence in the NMR relaxation rate $1/T_1$. Previous numerical studies have confirmed the RC behavior on the square lattice [11], as also shown in Fig. 5 of the present study. However, whether the frustrated triangular-

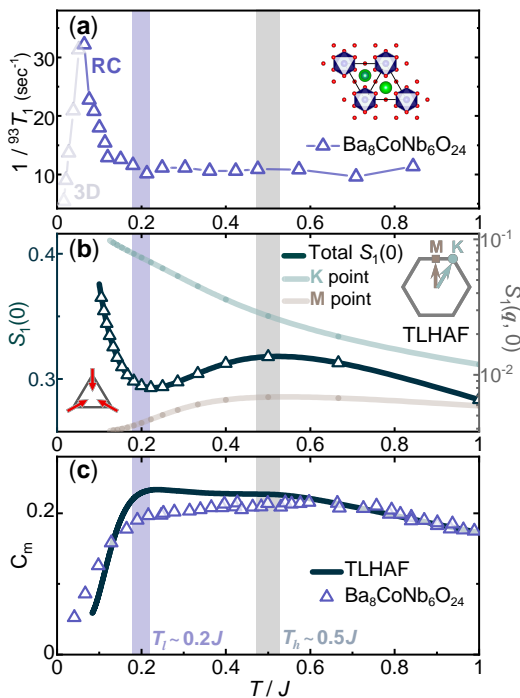


FIG. 7. (a) shows the experimental measurements of the spin-lattice relaxation $1/T_1$ on a triangular-lattice compound $\text{Ba}_8\text{CoNb}_6\text{O}_{24}$ [88], with the layered structure shown in the inset. (b) shows the calculated $S_1(0)$ of the TLHAF model on a YC 6×12 cylinder, including the $S_1(0)$ averaged on all \mathbf{q} points and that located at $\mathbf{q} = (\frac{2\pi}{3}, \frac{2\sqrt{3}\pi}{3})$ (K point) and $(0, \frac{2\sqrt{3}\pi}{3})$ (M point). (c) The lines represent calculated specific heat data and the triangle markers are the experimental data. The two shadow areas denote two temperature scales $T_h \simeq 0.5J$ and $T_l \simeq 0.2J$.

lattice system exhibits RC behavior and corresponding incipient magnetic order at low temperature remained unresolved.

To be specific, the triangular lattice HAF (TLHAF) magnet constitutes a prototypical frustrated system [90, 91] that has been originally proposed to host a QSL [3]. Subsequent investigations utilizing precise numerical methods have uncovered that the ground state of the system features a coplanar 120° magnetic order [92–94], which precludes the existence of a QSL state at absolute zero temperature. Nevertheless, from a finite-temperature perspective the system remains disordered and has a large magnetic entropy till low temperature [95, 96]. This thermodynamics anomaly has been noticed in early days [95] and confirmed more recently by diagrammatic Monte Carlo calculations [96]. The situation is dramatically different for the SLHAF system studied above (c.f., Fig. 5), the predicted RC behavior in TLHAF [89] has not been found in early numeric studies [95, 96].

Our TTN approach can also be applied to study the frustrated TLHAF quantum magnets, with the results shown in Fig. 7. Compared to those of the SLHAF in Fig. 5, where the $S_1(0)$ data increase exponentially in the RC regime, in Fig. 7(b) the $S_1(0)$ results of TLHAF remain flat, even slightly suppressed, for $T \lesssim T_h \simeq 0.5J$. The $S_1(0)$ data are found to be significantly enhanced only below $T_l \simeq 0.2J$.

With momentum resolution, in Fig. 5(b) we further show that $S_1(\mathbf{q} = \mathbf{K}, 0)$ increases monotonically as temperature lowers and becomes very prominent for $T \lesssim T_l$. This signals the onset of long-sought RC behaviors associated with three-sublattice order in the TLHAF system [50], and we find the spin-lattice relaxation $1/T_1$ provides a highly sensitive probe for the incipient order in both frustrated and unfrustrated HAF systems. Besides, the $S_1(0)$ results exhibit a maximum at the higher temperature scale T_h , which may be ascribed to the enhancement of $S_1(\mathbf{q} = \mathbf{M}, 0)$ due to activation of roton-like excitations [50] in the TLHAF system.

This theoretical insight significantly enhances our understanding of the recently studied TLHAF materials [88, 97–102]. In particular, the cobaltate compound $\text{Ba}_8\text{CoNb}_6\text{O}_{24}$, as reported in Refs. [88, 102], is considered an ideal realization of the TLHAF model due to its weak interlayer coupling and isotropic Heisenberg spin exchange. The NMR measurements have been conducted down to low temperature, and in Fig. 7(a) we show the experimental results adapted from Ref. [88], where the $1/T_1$ data of $\text{Ba}_8\text{CoNb}_6\text{O}_{24}$ level off even below $T_h \simeq 0.55J$ and fall into the RC scaling below $T_l \simeq 0.2J$, in striking similarity with model calculations shown in Fig. 7(b). In addition, the existence of two temperature scales, T_h and T_l , in TLHAF is also witnessed by the magnetic specific heat C_m shown in Fig. 7(c). Remarkably, the experimental C_m curve exhibits a hump at T_h and a shoulder at about T_l , in consistent with our TTN calculations on cylinders even with limited width [46].

C. Spin-lattice relaxation of the QSL candidates AYbCh_2

The triangular-lattice compound AYbCh_2 (with $A=\text{Na, K, Cs}$, and $\text{Ch} = \text{O, S, Se}$) has garnered significant attention in recent studies as a promising candidate for hosting QSL or proximate QSL on the triangular lattice [62–65, 103]. These compounds are believed to be described by an effective J_1 - J_2 model on the triangular lattice, where J_1 represents nearest-neighbor spin coupling, and J_2 is the next-nearest coupling [see Fig. 8(a)]. There are proposals using periodic table to tune the ratio J_2/J_1 in the compounds. For example, as shown in Fig. 8(a), NaYbO_2 and KYbSe_2 can have different coupling ratios that locate them in different regimes (ideally J_1 vs. proximate J_1 - J_2 QSL) of the phase diagram.

To examine the NMR signatures of possible QSL, in Fig. 8(b) we compute $S_1(0)$ for different coupling ratios J_2/J_1 , and find it shows distinctive behaviors in the ordered phase with $J_2/J_1 \lesssim 0.07$ and QSL regime with $0.07 \lesssim J_2/J_1 \lesssim 0.15$ [105, 106]. In Fig. 8(b), we show the NMR results of the compound NaYbO_2 , which corresponds to $J_2/J_1 \simeq 0$ [103], and find the relaxation rate $1/T_1$ increases rapidly at low temperature [104]. By comparing experimental results of NaYbO_2 and model calculations in Fig. 8(b), we find the measured spin-lattice relaxation $1/T_1$ suggest the presence of incipient order rather than QSL behaviors in NaYbO_2 , akin to $\text{Ba}_8\text{CoNb}_6\text{O}_{24}$ analyzed in Fig. 7. The characteristic temperature where $1/T_1$ starts to increase is about $T/J_{\text{NYO}} \approx 0.2$ for NaYbO_2 , very close to that of

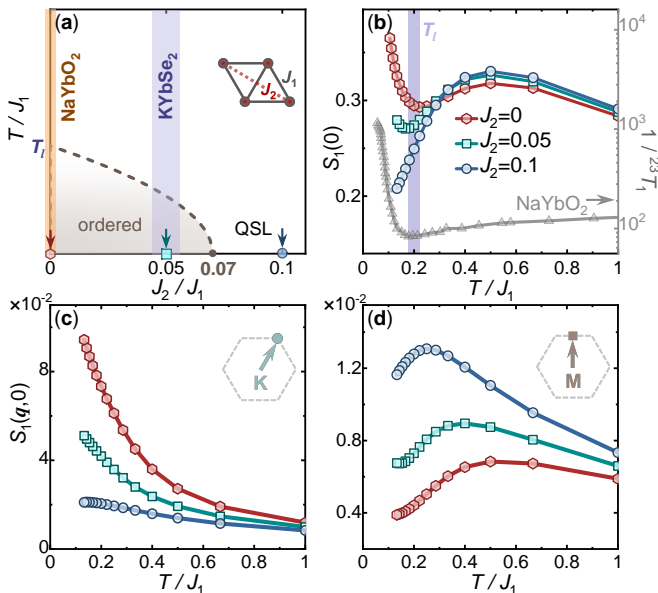


FIG. 8. (a) Sketch of J_1 - J_2 TLHAF phase diagram, where the two considered compounds NaYbO_2 and KYbSe_2 , as well as the three simulated parameters $J_2/J_1 = 0, 0.05, 0.1$, are also indicated. A quantum phase transition from the ordered phase to QSL occurs at $J_2/J_1 \simeq 0.07$. The inset shows the nearest-neighbor interaction J_1 and the next-nearest-neighbor interaction J_2 in a triangular lattice. The range of coupling ratio J_2/J_1 for KYbSe_2 is adapted from the estimation in Ref. [65], and $J_{\text{NYO}} \simeq 5.5$ K of NaYbO_2 from Ref. [103]. (b) shows the calculated $S_1(0)$ of the J_1 - J_2 TLHAF model on a $YC 6 \times 12$ cylinder, and compares the results to the experimental $1/T_1$ data measured on NaYbO_2 [104]. (c) and (d) present the calculated $S_1(\mathbf{q}, 0)$ at the \mathbf{K} and \mathbf{M} points in the BZ (see insets), respectively.

pure TLHAF model and indeed suggesting a negligible J_2 in the compound.

We further increase J_2 coupling and find the low- T values of $S_1(0)$ gets suppressed and the incipient order characteristic temperature also decreased. For $J_2/J_1 = 0.05$ that corresponds to KYbSe_2 [65], we find the low-temperature increase in NMR relaxation rate is only modest, suggesting the proximity to QSL. For $J_2 = 0.1$ case well located in the QSL phase, we observe decreasing $S_1(0)$ as temperature lowers, following approximately an algebraic scaling that reflects a gapless nature of the QSL [107, 108]. This echoes the previous $1/T_1$ measurements on possible Dirac QSL materials [109]. To clarify the contributions from different \mathbf{q} points in the BZ, we show in Fig. 8(c,d) the simulated $S_1(\mathbf{q}, 0)$ with $\mathbf{q} = \mathbf{K}, \mathbf{M}$. In Fig. 8(c), we observe that $S_1(\mathbf{K}, 0)$ gets suppressed at low temperature and the divergence behaviors due to incipient order no longer exist. On the other hand, the relaxation rate $S_1(\mathbf{M}, 0)$ gets enhanced in Fig. 8(d), reflecting softening of the spin excitations at \mathbf{M} point. This is consistent with previous dynamical study of J_1 - J_2 TLHAF [110], where both \mathbf{K} and \mathbf{M} points are shown to be gapless. Therefore, our findings not only present a numerical approach for assessing $S_{1,2}(0)$ and recognizing dynamical trait of geometric frustration, but also underscore the potential of NMR relaxation as

a highly sensitive diagnostic tool for probing the QSL state in the AYbCh_2 family.

V. DISCUSSIONS AND OUTLOOK

Essential for identifying exotic quantum spin states and emergent phenomena, low-energy excitations and spin fluctuations can be sensitively probed by spectroscopic techniques like NMR. However, numerical simulations of the temperature-dependent dynamical fluctuations, such as those characterized by the low-frequency dynamical spin structure $S(0) \sim 1/T_1$ vs. T , remained challenging to compute.

In this work, we demonstrate that the TTN — a powerful approach for calculating equilibrium properties at finite temperature [36, 37, 39–42, 46–48] — can also simulate the NMR relaxation rate $1/T_1$, with spatial, momentum, and spin resolutions. The approach can be used to compute proxies $S_{1,2}(\omega = 0)$ with both high accuracy and controllability. In addition to spin-lattice relaxation $1/T_1$, our TTN approach can also compute the spin-spin relaxation rate $1/T_{2G}$, leveraging the calculations of imaginary-time correlators. Our method enables extract extractions of the critical exponents (η and $z\nu$), recognition of topological edge modes, incipient orders, and the possible QSL phase, among others, without the need for the somewhat ill-posed analytical continuation or other complex dynamical approaches.

It thus offers us a very useful tool for analyzing the NMR experiments on realistic compounds, particularly the QSL candidates with high degree of spin frustration. For the spin-chain compound CoNb_2O_6 , the NMR results show an universal scaling $S_1^{zz}(\omega = 0) \sim 1/T_1 \propto T^{-3/4}$ and determined critical exponent $z\nu \simeq 1$ through the data-collapse analysis inspired by the numerical results. For the TLHAF compound $\text{Ba}_8\text{CoNb}_6\text{O}_{24}$, we find the low-temperature scale for incipient spin order is evident from the $1/T_1$ measurements. The AYbSe_2 family on the J_1 - J_2 triangular lattice has been intensively studied in experiments, and our calculations provide valuable insights into their spin dynamics and useful guidance for exploring possible QSL in these compounds.

In summary, our results highlight the importance of developing theoretical tools for low-energy spectroscopic properties for investigating quantum magnets. Above we use the MPO-based TTN approach to simulate infinite-size 1D chain and also large-scale 2D cylinder geometries, and showcase the power of our approach with representative model examples and realistic materials. Moreover, such a TTN approach can be generalized to infinite 2D systems using the projected entangled pair operator [111]. Beyond the quantum spin systems, the TTN proxy can also be employed to study the many-electron problems, which are important for understanding the NMR measurements on correlated electron materials, which we leave for future studies.

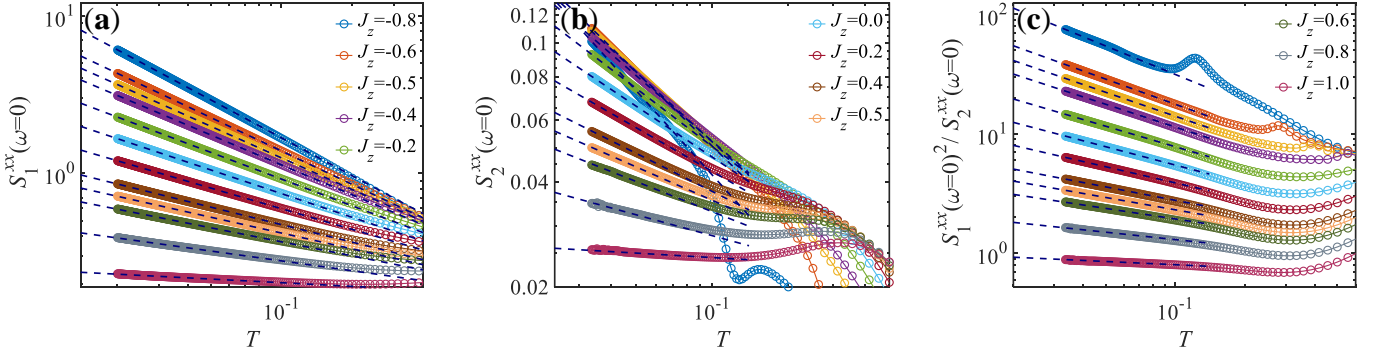


FIG. A1. **Supporting data of $\mathcal{S}_1(0)$ in the TLL phase of the spin-1/2 HAF chain.** We provide three different proxies to compute $1/T_1$ in the TLL phase, including (a) $\mathcal{S}_1^{xx}(0)$, (b) $\mathcal{S}_2^{xx}(0)$, and (c) $[\mathcal{S}_1^{xx}(0)]^2/\mathcal{S}_2^{xx}(0)$. The dashed lines are power-law fittings $1/T_1^{xx} \sim T^{\eta-1}$ at low temperature, from which the corresponding exponents η obtained in three proxy simulations are found to be consistent. The fitted exponents η are shown in the inset of Fig. 2(a) in the main text.

VI. ACKNOWLEDGMENTS

The authors are indebted to Lei Wang, Yang Qi, Jiahao Yang, Yuchen Fan, and Weiqiang Yu for helpful discussions. This work was supported by the National Natural Science Foundation of China (Grant Nos. 12222412, 12347138, 12047503, 12334008 and 12174441), the National Key Projects for Research and Development of China (Grant Nos. 2023YFA1406500 and 2021YFA1400400), China Postdoctoral Science Foundation (Grant No. 2021TQ0355), and CAS Project for Young Scientists in Basic Research (Grant No. YSBR-057). We thank HPC at ITP-CAS and RUC for the technical support and generous allocation of CPU time.

Appendix A: Thermal Tensor Network Approach

In this appendix, we review the thermal tensor network method that was employed to derive the equilibrium density operator and the imaginary time proxies associated with spin relaxation, specifically $1/T_1$ or spectral weight $\mathcal{S}_1(\omega = 0)$, for correlated quantum spin systems.

1. Linearized tensor renormalization group

We employ linearized tensor renormalization group (LTRG) method to simulate infinite-size and finite-size 1D quantum spin chains [41]. The thermodynamics calculations resort to an efficient contraction of the (1+1)D TTN through the Trotter-Suzuki decomposition. Through (first-order) Trotter-Suzuki decomposition, the density matrix $\rho = [\exp(-\tau H)]^N$ can be expressed as

$$\rho \approx \sum_{\{\sigma_i^n\}} \prod_{i=1}^L \prod_{n=1}^N \nu_{\sigma_i^n, \sigma_{i+1}^n, \sigma_i^{n+1}, \sigma_{i+1}^{n+1}}, \quad (\text{A1})$$

by inserting N sets of orthonormal basis $\{\sigma_i^n\}$ where i is spatial index and n the imaginary-time index. We arrive at a TTN

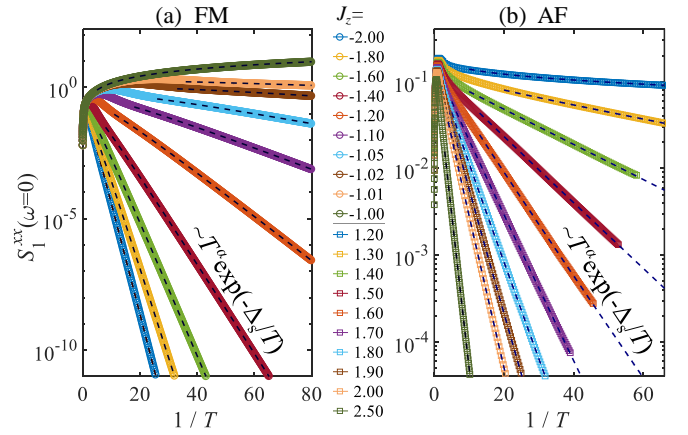


FIG. A2. **Supporting data of $\mathcal{S}_1(0)$ in the gapped phase of the spin-1/2 HAF chain.** The calculated $\mathcal{S}_1^{xx}(\omega = 0)$ results and their exponential fittings in (a) FM and (b) AF phases of the easy-axis spin-1/2 HAF chain.

consists of rank-four tensors,

$$\nu_{\sigma_i^n, \sigma_{i+1}^n, \sigma_i^{n+1}, \sigma_{i+1}^{n+1}} = \langle \sigma_i^n, \sigma_{i+1}^n | e^{-\tau h_i} | \sigma_i^{n+1}, \sigma_{i+1}^{n+1} \rangle, \quad (\text{A2})$$

To contract the TTN, we start from an identity MPO which represents the density matrix at infinite high temperature ($\beta = 0$), and iteratively project ν tensors onto the MPO. The system cools down from $\beta = 0$ to various lower temperatures, following a linear inverse-temperature grid, i.e., $\beta = n\tau$ at n -th step.

In practical calculations, we regard the MPO as a super vector and follows the decimation technique developed for matrix product state [38, 41, 45]. To further reduce the Trotter errors, we employ up to sixth-order Trotter-Suzuki decomposition so that the Trotter error is less than numerical precision and can be ignored in our calculations. Besides, the step length τ can also be adjusted dynamically during the cooling process, with the temperature grid also quite flexible.

2. Tensor renormalization group for 2D lattice models

We exploit exponential (XTRG) [46] and tangent-space (tanTRG) [48] tensor renormalization group to simulate 2D quantum spin models. In XTRG calculations, we start from the initial density matrix $\rho_0(\tau)$ at a very high temperature with $\tau = \mathcal{O}(10^{-4})$ ($T \equiv 1/\tau$), represented in an MPO form via a series expansion [44]

$$\rho_0(\tau) = e^{-\tau H} = \sum_{n=0}^{\infty} \frac{(-\tau H)^n}{n!} \simeq \sum_{n=0}^{N_{\text{cut}}} \frac{(-\tau H)^n}{n!}. \quad (\text{A3})$$

For a high temperature such as $\tau = 2.5 \times 10^{-4}$, the expansion error is with machine precision for $N_{\text{cut}} = 6-7$. Subsequently, by keeping squaring the density matrix repeatedly, i.e.,

$$\rho_n(2^n \tau) \cdot \rho_n(2^n \tau) \rightarrow \rho_{n+1}(2^{n+1} \tau),$$

we cool down the system along a logarithmic inverse-temperature grid $\tau \rightarrow 2\tau \rightarrow 2^2\tau \rightarrow \dots \rightarrow 2^n\tau$. Such a cooling process reaches low temperature exponentially fast, with the projection and truncation steps significantly reduced. This renders higher accuracy than traditional linear evolution scheme, particularly for the challenging 2D lattice models. Thus it constitutes a very powerful TTN method for ultra-low temperature simulations.

In tanTRG simulations, on the other hand, we consider the imaginary-time evolution of density matrix $\rho(\beta)$

$$\frac{d\rho}{d\beta} = -H\rho. \quad (\text{A4})$$

In the tensor-network language, we prepare the density matrix $\rho = e^{-\beta H}$ and the Hamiltonian H in the MPO form, and Eq. A4 can be solved by the tangent-space technique [69, 112, 113] by introducing a Choi transformation [114]

$$\frac{d}{d\beta} |\rho\rangle\rangle = -H \otimes I |\rho\rangle\rangle. \quad (\text{A5})$$

Noticing that $e^{-\beta H \otimes I} = e^{-\beta H} \otimes I$, we solve Eq. A5 within the MPO form [48].

With tanTRG, we reduce the computational complexity from $\mathcal{O}(D^4)$ of XTRG to $\mathcal{O}(D^3)$, which allows us to retain much larger bond dimension in MPO. Thus, for challenging problems like the triangular lattice HAF model with width $W = 6$, tanTRG is employed so we can retain up to 16,000 U(1) states [4000 SU(2) multiplets] to obtain converged results.

Appendix B: Supplemental Results of Spin Lattice Models

1. Spin-1/2 Heisenberg chain

We start with more detailed $\mathcal{S}_{1,2}(\omega = 0)$ results of the spin-1/2 HAF chains, with the results shown in Figs. A1, A2, A3.

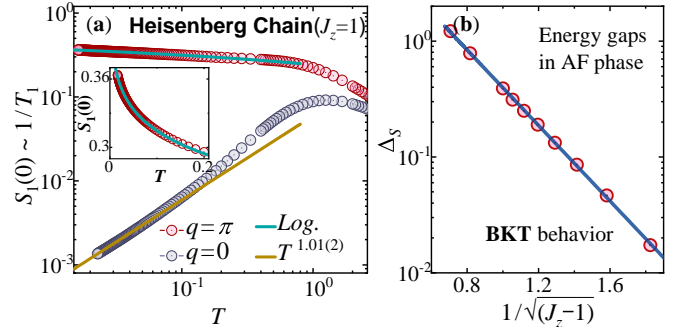


FIG. A3. **Calculated $\mathcal{S}_1(0)$ near the isotropic spin-1/2 HAF chain.** (a) The $\mathcal{S}_1(q, \omega = 0)$ of the isotropic HAF chain ($J_z = 1$) for two different moments $q = 0$ and π , respectively, which show distinct behaviors as indicated by the two solid lines. The uniform $q = 0$ contribution scales linearly with T , while the staggered $q = \pi$ part is nearly a constant with a logarithmic correction (see texts below). The inset demonstrates a zoomed-in linear plot of the data with $q = \pi$ at low temperatures. (b) The exponential gap opening that indicates a BKT transition from the gapless TLL to the gapped AF phase.

In the main text, we have illustrated that the critical exponent η varies as J_z is altered within the TLL phase [c.f., in Fig. 2(a)]. To support this conclusion, we show in Fig. A1 the calculated results for $\mathcal{S}_1^{xx}(\omega = 0)$, $\mathcal{S}_2^{xx}(\omega = 0)$, and the ratio $[\mathcal{S}_1^{xx}(\omega = 0)]^2 / \mathcal{S}_2^{xx}(\omega = 0)$ alongside their respective power-law fits in low temperatures. We find the three approaches generate consistent results. In Fig. A2, we show the computed $\mathcal{S}_1^{xx}(\omega = 0)$ and their fittings at low temperatures, given by $T^\alpha \exp(\Delta_S/T)$, for the gapped FM and AF phases. From the fittings, we determine the values of spin gaps and present the results in Fig. 2(a) of the main text.

For the spin-1/2 XXZ chain, the Heisenberg point $J_z = 1$ with SU(2) symmetry separates the gapped AF and gapless TLL phases. Figure A3(a) demonstrates distinct behaviors of $\mathcal{S}_1^{xx}(q, \omega = 0)$ at $q = 0$ (representing long-wave length fluctuations) and $q = \pi$ (staggered moment fluctuations) for the Heisenberg chain. Specifically, for $q = 0$ it corresponding to $\eta = 2$ and thus $\mathcal{S}_1^{xx}(\omega = 0, q = 0) \propto T$. On the other hand, for $q = \pi$, the staggered fluctuations dominates and are nearly constant (with a multiplicative logarithmic correction) at low temperature [8, 10]. The behavior of $\mathcal{S}_1^{xx}(\omega = 0, q = \pi)$ is fitted with the formula, $\sqrt{\ln(\Lambda/T) + \ln(\sqrt{\ln(\Lambda/T)})}$ with $\Lambda \simeq 24.3$ [22]. The logarithmic correction can be ascribed to the presence of marginally irrelevant operator in critical HAF chain [8]. In Fig. A3(b) we show the spin gap Δ_S vs. $1/\sqrt{(J_z - 1)}$, from which we observe $\Delta_S \sim e^{-\xi/\sqrt{(J_z - 1)}}$ with ξ a constant. The exponential opening of spin gap reveals the existence of Berezinskii-Kosterlitz-Thouless transition at the isotropic Heisenberg point.

2. Transverse-field Ising model on the square lattice

In Fig. A4, we present supplementary data on $\mathcal{S}_1(\omega = 0)$ for the TFI model on the square lattice, with the focus on the

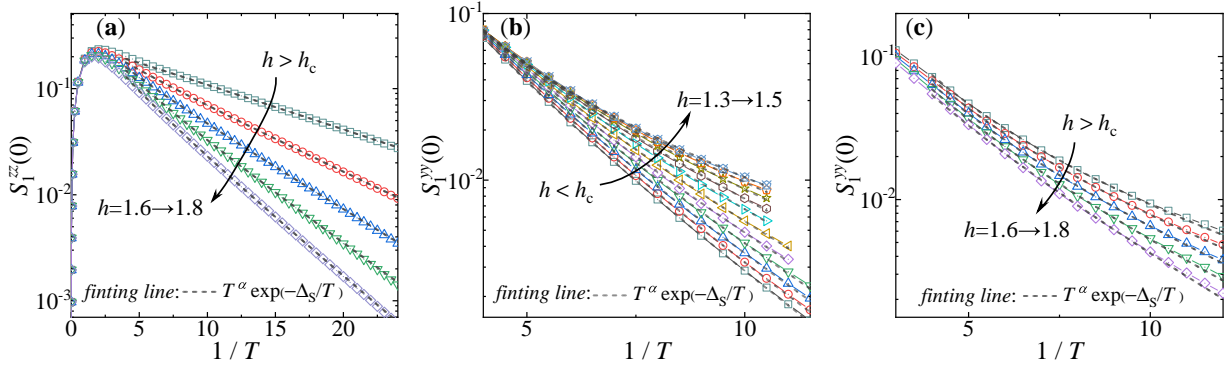


FIG. A4. **Spin-lattice relaxation rate of TFI model on the square lattice.** The calculated results of (a) $S_1^{zz}(\omega = 0)$ and (b-c) $S_1^{yy}(\omega = 0)$ for the square-lattice TFI model in the gapped phases. The results are found to show exponential decaying behaviors, and the fittings to the results are indicated by the dashed lines. The estimated gaps Δ_S are collected and plotted in Fig. 4(b) of the main text.

gapped paramagnetic ($h > h_c$) and ordered states ($h < h_c$) in the vicinity of field-driven Ising QCP. In Fig. A4, we show the calculated $S_1^{zz}(\omega = 0)$ for $h > h_c$ (panel a) and $S_1^{yy}(\omega = 0)$ for both $h > h_c$ (panel b) and $h < h_c$ (panel c), along with the exponential fittings at low temperatures, following

the expression $S_1 \sim T^\alpha \exp(-\Delta_S/T)$, to extract the spin gap Δ_S . From the results in Fig. A4, we see the gap becomes increased as h deviates h_c . By collecting the fitted values of Δ_S , we show the gaps in Fig. 4(c) of the main text, which fall into algebraic scaling vs. $|h - h_c|$.

-
- [1] J. Xiang, C. Zhang, Y. Gao, W. Schmidt, K. Schmalzl, C.-W. Wang, B. Li, N. Xi, X.-Y. Liu, H. Jin, G. Li, J. Shen, Z. Chen, Y. Qi, Y. Wan, W. Jin, W. Li, P. Sun, and G. Su, Giant magnetocaloric effect in spin supersolid candidate $\text{Na}_2\text{BaCo}(\text{PO}_4)_2$, *Nature* **625**, 270 (2024).
- [2] Y. Shangguan, S. Bao, Z.-Y. Dong, N. Xi, Y.-P. Gao, Z. Ma, W. Wang, Z. Qi, S. Zhang, Z. Huang, J. Liao, X. Zhao, B. Zhang, S. Cheng, H. Xu, D. Yu, R. A. Mole, N. Murai, S. Ohira-Kawamura, L. He, J. Hao, Q.-B. Yan, F. Song, W. Li, S.-L. Yu, J.-X. Li, and J. Wen, A one-third magnetization plateau phase as evidence for the Kitaev interaction in a honeycomb-lattice antiferromagnet, *Nature Physics* **19**, 1883 (2023).
- [3] P. W. Anderson, Resonating valence bonds: A new kind of insulator?, *Mater. Res. Bull.* **8**, 153 (1973).
- [4] L. Balents, Spin liquids in frustrated magnets, *Nature* **464**, 199 (2010).
- [5] Y. Zhou, K. Kanoda, and T.-K. Ng, Quantum spin liquid states, *Rev. Mod. Phys.* **89**, 025003 (2017).
- [6] C. Broholm, R. J. Cava, S. A. Kivelson, D. G. Nocera, M. R. Norman, and T. Senthil, Quantum spin liquids, *Science* **367**, eaay0668 (2020).
- [7] M. Takigawa, N. Motoyama, H. Eisaki, and S. Uchida, Dynamics in the $S = 1/2$ one-dimensional antiferromagnet Sr_2CuO_3 via ^{63}Cu NMR, *Phys. Rev. Lett.* **76**, 4612 (1996).
- [8] S. Sachdev, NMR relaxation in half-integer antiferromagnetic spin chains, *Phys. Rev. B* **50**, 13006 (1994).
- [9] J. Steinberg, N. P. Armitage, F. H. L. Essler, and S. Sachdev, NMR relaxation in Ising spin chains, *Phys. Rev. B* **99**, 035156 (2019).
- [10] A. W. Sandvik, NMR relaxation rates for the spin-1/2 Heisenberg chain, *Phys. Rev. B* **52**, R9831 (1995).
- [11] A. W. Sandvik and D. J. Scalapino, Spin dynamics of La_2CuO_4 and the two-dimensional Heisenberg model, *Phys. Rev. B* **51**, 9403 (1995).
- [12] F. Naef and X. Wang, Nuclear spin relaxation rates in two-leg spin ladders, *Phys. Rev. Lett.* **84**, 1320 (2000).
- [13] A. W. Kinross, M. Fu, T. J. Munsie, H. A. Dabkowska, G. M. Luke, S. Sachdev, and T. Imai, Evolution of quantum fluctuations near the quantum critical point of the transverse field Ising chain system CoNb_2O_6 , *Phys. Rev. X* **4**, 031008 (2014).
- [14] Y. Cui, H. Zou, N. Xi, Z. He, Y. X. Yang, L. Shu, G. H. Zhang, Z. Hu, T. Chen, R. Yu, J. Wu, and W. Yu, Quantum criticality of the Ising-like screw chain antiferromagnet $\text{SrCo}_2\text{V}_2\text{O}_8$ in a transverse magnetic field, *Phys. Rev. Lett.* **123**, 067203 (2019).
- [15] H. Zou, Y. Cui, X. Wang, Z. Zhang, J. Yang, G. Xu, A. Okutani, M. Hagiwara, M. Matsuda, G. Wang, G. Mussardo, K. Hódsági, M. Kormos, Z. He, S. Kimura, R. Yu, W. Yu, J. Ma, and J. Wu, E_g spectra of quasi-one-dimensional antiferromagnet $\text{BaCo}_2\text{V}_2\text{O}_8$ under transverse field, *Phys. Rev. Lett.* **127**, 077201 (2021).
- [16] Z. Hu, Z. Ma, Y.-D. Liao, H. Li, C. Ma, Y. Cui, Y. Shangguan, Z. Huang, Y. Qi, W. Li, Z. Y. Meng, J. Wen, and W. Yu, Evidence of the Berezinskii-Kosterlitz-Thouless phase in a frustrated magnet, *Nat. Commun.* **11**, 5631 (2020).
- [17] J. Zheng, K. Ran, T. Li, J. Wang, P. Wang, B. Liu, Z.-X. Liu, B. Normand, J. Wen, and W. Yu, Gapless spin excitations in the field-induced quantum spin liquid phase of $\alpha\text{-RuCl}_3$, *Phys. Rev. Lett.* **119**, 227208 (2017).
- [18] Y. Cui, L. Liu, H. Lin, K.-H. Wu, W. Hong, X. Liu, C. Li, Z. Hu, N. Xi, S. Li, R. Yu, A. W. Sandvik, and W. Yu, Proximate deconfined quantum critical point in $\text{SrCu}_2(\text{BO}_3)_2$, *Science* **380**, 1179 (2023).
- [19] H. Li, Y. D. Liao, B.-B. Chen, X.-T. Zeng, X.-L. Sheng, Y. Qi, Z. Y. Meng, and W. Li, Kosterlitz-Thouless melting of magnetic order in the triangular quantum Ising material TmMgGaO_4 , *Nat. Commun.* **11**, 1111 (2020).
- [20] J. Wang, H. Li, N. Xi, Y. Gao, Q.-B. Yan, W. Li, and G. Su, Plaquette singlet transition, magnetic barocaloric effect, and

- spin supersolidity in the Shastry-Sutherland model, *Phys. Rev. Lett.* **131**, 116702 (2023).
- [21] J. Yang, W. Yuan, T. Imai, Q. Si, J. Wu, and M. Kormos, Local dynamics and thermal activation in the transverse-field Ising chain, *Phys. Rev. B* **106**, 125149 (2022).
- [22] V. Barzykin, NMR relaxation rates in a spin- $\frac{1}{2}$ antiferromagnetic chain, *Phys. Rev. B* **63**, 140412 (2001).
- [23] M. Dupont, S. Capponi, and N. Laflorencie, Temperature dependence of the NMR relaxation rate $1/T_1$ for quantum spin chains, *Phys. Rev. B* **94**, 144409 (2016).
- [24] E. Coira, P. Barmettler, T. Giamarchi, and C. Kollath, Temperature dependence of the NMR spin-lattice relaxation rate for spin- $\frac{1}{2}$ chains, *Phys. Rev. B* **94**, 144408 (2016).
- [25] S. Capponi, M. Dupont, A. W. Sandvik, and P. Sengupta, NMR relaxation in the spin-1 heisenberg chain, *Phys. Rev. B* **100**, 094411 (2019).
- [26] B. Bertini, F. Heidrich-Meisner, C. Karrasch, T. Prosen, R. Steinigeweg, and M. Žnidarič, Finite-temperature transport in one-dimensional quantum lattice models, *Rev. Mod. Phys.* **93**, 025003 (2021).
- [27] Y.-R. Shu, M. Dupont, D.-X. Yao, S. Capponi, and A. W. Sandvik, Dynamical properties of the $S = \frac{1}{2}$ random Heisenberg chain, *Phys. Rev. B* **97**, 104424 (2018).
- [28] W. Tang, H.-H. Tu, and L. Wang, Continuous matrix product operator approach to finite temperature quantum states, *Phys. Rev. Lett.* **125**, 170604 (2020).
- [29] C. Huscroft, R. Gass, and M. Jarrell, Maximum entropy method of obtaining thermodynamic properties from quantum Monte Carlo simulations, *Phys. Rev. B* **61**, 9300 (2000).
- [30] H. Shao, Y. Q. Qin, S. Capponi, S. Chesi, Z. Y. Meng, and A. W. Sandvik, Nearly deconfined spinon excitations in the square-lattice spin-1/2 Heisenberg antiferromagnet, *Phys. Rev. X* **7**, 041072 (2017).
- [31] L. Huang and S. Liang, Stochastic pole expansion method (2023), [arXiv:2307.11324](https://arxiv.org/abs/2307.11324).
- [32] L. Huang and S. Liang, Reconstructing lattice qcd spectral functions with stochastic pole expansion and nevanlinna analytic continuation (2023), [arXiv:2309.11114](https://arxiv.org/abs/2309.11114).
- [33] J. Fei, C.-N. Yeh, and E. Gull, Nevanlinna analytical continuation, *Phys. Rev. Lett.* **126**, 056402 (2021).
- [34] M. Randeria, N. Trivedi, A. Moreo, and R. T. Scalettar, Pairing and spin gap in the normal state of short coherence length superconductors, *Phys. Rev. Lett.* **69**, 2001 (1992).
- [35] Y. Fan, J. Yang, W. Yu, J. Wu, and R. Yu, Phase diagram and quantum criticality of Heisenberg spin chains with Ising anisotropic interchain couplings, *Phys. Rev. Res.* **2**, 013345 (2020).
- [36] R. J. Bursill, T. Xiang, and G. A. Gehring, The density matrix renormalization group for a quantum spin chain at non-zero temperature, *J. Phys.: Condens. Matter* **8**, L583 (1996).
- [37] X. Wang and T. Xiang, Transfer-matrix density-matrix renormalization-group theory for thermodynamics of one-dimensional quantum systems, *Phys. Rev. B* **56**, 5061 (1997).
- [38] M. Zwolak and G. Vidal, Mixed-state dynamics in one-dimensional quantum lattice systems: A time-dependent superoperator renormalization algorithm, *Phys. Rev. Lett.* **93**, 207205 (2004).
- [39] A. E. Feiguin and S. R. White, Finite-temperature density matrix renormalization using an enlarged hilbert space, *Phys. Rev. B* **72**, 220401(R) (2005).
- [40] S. R. White, Minimally entangled typical quantum states at finite temperature, *Phys. Rev. Lett.* **102**, 190601 (2009).
- [41] W. Li, S.-J. Ran, S.-S. Gong, Y. Zhao, B. Xi, F. Ye, and G. Su, Linearized tensor renormalization group algorithm for the calculation of thermodynamic properties of quantum lattice models, *Phys. Rev. Lett.* **106**, 127202 (2011).
- [42] P. Czarnik, L. Cincio, and J. Dziarmaga, Projected entangled pair states at finite temperature: Imaginary time evolution with ancillas, *Phys. Rev. B* **86**, 245101 (2012).
- [43] P. Czarnik and J. Dziarmaga, Variational approach to projected entangled pair states at finite temperature, *Phys. Rev. B* **92**, 035152 (2015).
- [44] B.-B. Chen, Y.-J. Liu, Z. Chen, and W. Li, Series-expansion thermal tensor network approach for quantum lattice models, *Phys. Rev. B* **95**, 161104(R) (2017).
- [45] Y.-L. Dong, L. Chen, Y.-J. Liu, and W. Li, Bilayer linearized tensor renormalization group approach for thermal tensor networks, *Phys. Rev. B* **95**, 144428 (2017).
- [46] B.-B. Chen, L. Chen, Z. Chen, W. Li, and A. Weichselbaum, Exponential Thermal Tensor Network Approach for Quantum Lattice Models, *Phys. Rev. X* **8**, 031082 (2018).
- [47] A. Kshetrimayum, M. Rizzi, J. Eisert, and R. Orús, Tensor network annealing algorithm for two-dimensional thermal states, *Phys. Rev. Lett.* **122**, 070502 (2019).
- [48] Q. Li, Y. Gao, Y.-Y. He, Y. Qi, B.-B. Chen, and W. Li, Tangent space approach for thermal tensor network simulations of the 2D Hubbard model, *Phys. Rev. Lett.* **130**, 226502 (2023).
- [49] H. Li, B.-B. Chen, Z. Chen, J. von Delft, A. Weichselbaum, and W. Li, Thermal tensor renormalization group simulations of square-lattice quantum spin models, *Phys. Rev. B* **100**, 045110 (2019).
- [50] L. Chen, D.-W. Qu, H. Li, B.-B. Chen, S.-S. Gong, J. von Delft, A. Weichselbaum, and W. Li, Two-temperature scales in the triangular-lattice Heisenberg antiferromagnet, *Phys. Rev. B* **99**, 140404(R) (2019).
- [51] B.-B. Chen, C. Chen, Z. Chen, J. Cui, Y. Zhai, A. Weichselbaum, J. von Delft, Z. Y. Meng, and W. Li, Quantum Many-Body Simulations of the Two-Dimensional Fermi-Hubbard Model in Ultracold Optical Lattices, *Phys. Rev. B* **103**, L041107 (2021).
- [52] X. Lin, B.-B. Chen, W. Li, Z. Y. Meng, and T. Shi, Exciton proliferation and fate of the topological mott insulator in a twisted bilayer graphene lattice model, *Phys. Rev. Lett.* **128**, 157201 (2022).
- [53] T. Liu, X.-Y. Liu, Y. Gao, H. Jin, J. He, X.-L. Sheng, W. Jin, Z. Chen, and W. Li, Significant inverse magnetocaloric effect induced by quantum criticality, *Phys. Rev. Research* **3**, 033094 (2021).
- [54] S. Yu, Y. Gao, B.-B. Chen, and W. Li, Learning the effective spin hamiltonian of a quantum magnet, *Chin. Phys. Lett.* **38**, 097502 (2021).
- [55] H. Li, Y. D. Liao, B.-B. Chen, X.-T. Zeng, X.-L. Sheng, Y. Qi, Z. Y. Meng, and W. Li, Kosterlitz-Thouless melting of magnetic order in the triangular quantum Ising material TmMgGaO₄, *Nat. Commun.* **11**, 1111 (2020).
- [56] X.-Y. Liu, Y. Gao, H. Li, W. Jin, J. Xiang, H. Jin, Z. Chen, W. Li, and G. Su, Quantum spin liquid candidate as superior refrigerant in cascade demagnetization cooling, *Communications Physics* **5**, 233.
- [57] Y. Gao, Y.-C. Fan, H. Li, F. Yang, X.-T. Zeng, X.-L. Sheng, R. Zhong, Y. Qi, Y. Wan, and W. Li, Spin supersolidity in nearly ideal easy-axis triangular quantum antiferromagnet Na₂BaCo(PO₄)₂, *npj Quantum Materials* **7**, 89.
- [58] H. Li, D.-W. Qu, H.-K. Zhang, Y.-Z. Jia, S.-S. Gong, Y. Qi, and W. Li, Universal thermodynamics in the Kitaev fractional liquid, *Phys. Rev. Research* **2**, 043015 (2020).
- [59] H. Li, H.-K. Zhang, J. Wang, H.-Q. Wu, Y. Gao, D.-W. Qu, Z.-X. Liu, S.-S. Gong, and W. Li, Identification of magnetic

- interactions and high-field quantum spin liquid in α - RuCl_3 , *Nat. Commun.* **12**, 4007 (2021).
- [60] H. Li, W. Li, and G. Su, High-field quantum spin liquid transitions and angle-field phase diagram of the Kitaev magnet α - RuCl_3 , *Phys. Rev. B* **107**, 115124 (2023).
- [61] X.-G. Zhou, H. Li, Y. H. Matsuda, A. Matsuo, W. Li, N. Kurita, G. Su, K. Kindo, and H. Tanaka, Possible intermediate quantum spin liquid phase in α - RuCl_3 under high magnetic fields up to 100 T, *Nat. Commun.* **14**, 5630 (2023).
- [62] W. Liu, Z. Zhang, J. Ji, Y. Liu, J. Li, X. Wang, H. Lei, G. Chen, and Q. Zhang, Rare-earth Chalcogenides: A large family of triangular lattice spin liquid candidates, *Chinese Physics Letters* **35**, 117501 (2018).
- [63] K. M. Ranjith, S. Luther, T. Reimann, B. Schmidt, P. Schlander, J. Sichelschmidt, H. Yasuoka, A. M. Strydom, Y. Skourski, J. Wosnitza, H. Kühne, T. Doert, and M. Baenitz, Anisotropic field-induced ordering in the triangular-lattice quantum spin liquid NaYbSe_2 , *Phys. Rev. B* **100**, 224417 (2019).
- [64] P.-L. Dai, G. Zhang, Y. Xie, C. Duan, Y. Gao, Z. Zhu, E. Feng, Z. Tao, C.-L. Huang, H. Cao, A. Podlesnyak, G. E. Granroth, M. S. Everett, J. C. Neuefeind, D. Voneshen, S. Wang, G. Tan, E. Morosan, X. Wang, H.-Q. Lin, L. Shu, G. Chen, Y. Guo, X. Lu, and P. Dai, Spinon fermi surface spin liquid in a triangular lattice antiferromagnet NaYbSe_2 , *Phys. Rev. X* **11**, 021044 (2021).
- [65] A. O. Scheie, E. A. Ghioldi, J. Xing, J. A. M. Paddison, N. E. Sherman, M. Dupont, L. D. Sanjeeva, S. Lee, A. J. Woods, D. Abernathy, D. M. Pajerowski, T. J. Williams, S.-S. Zhang, L. O. Manuel, A. E. Trumper, C. D. Pemmaraju, A. S. Sefat, D. S. Parker, T. P. Devereaux, R. Movshovich, J. E. Moore, C. D. Batista, and D. A. Tennant, Proximate spin liquid and fractionalization in the triangular antiferromagnet KYbSe_2 , *Nature Physics* **20**, 74 (2024).
- [66] H. W. J. Blöte and Y. Deng, Cluster Monte Carlo simulation of the transverse Ising model, *Phys. Rev. E* **66**, 066110 (2002).
- [67] N. Wiebe, D. Berry, P. Hoyer, and B. C. Sanders, Higher order decompositions of ordered operator exponentials, *J. Phys. A: Math. Theor.* **43**, 065203 (2010).
- [68] D.-W. Qu, B.-B. Chen, X. Lu, Q. Li, Y. Qi, S.-S. Gong, W. Li, and G. Su, d -wave superconductivity, pseudogap, and the phase diagram of t - t' - J model at finite temperature (2023), [arXiv:2211.06322](https://arxiv.org/abs/2211.06322).
- [69] J. Haegeman, J. I. Cirac, T. J. Osborne, I. Pižorn, H. Verschelde, and F. Verstraete, Time-dependent variational principle for quantum lattices, *Phys. Rev. Lett.* **107**, 070601 (2011).
- [70] L. Hackl, T. Guaita, T. Shi, J. Haegeman, E. Demler, and J. I. Cirac, Geometry of variational methods: dynamics of closed quantum systems, *SciPost Phys.* **9**, 048 (2020).
- [71] E. Fradkin, *Field Theories of Condensed Matter Physics*, 2nd ed. (Cambridge University Press, 2013).
- [72] W. Hong, L. Liu, C. Liu, X. Ma, A. Koda, X. Li, J. Song, W. Yang, J. Yang, P. Cheng, H. Zhang, W. Bao, X. Ma, D. Chen, K. Sun, W. Guo, H. Luo, A. W. Sandvik, and S. Li, Extreme suppression of antiferromagnetic order and critical scaling in a two-dimensional random quantum magnet, *Phys. Rev. Lett.* **126**, 037201 (2021).
- [73] A. Luther and I. Peschel, Calculation of critical exponents in two dimensions from quantum field theory in one dimension, *Phys. Rev. B* **12**, 3908 (1975).
- [74] S. R. White and D. A. Huse, Numerical renormalization-group study of low-lying eigenstates of the antiferromagnetic $S=1$ Heisenberg chain, *Phys. Rev. B* **48**, 3844 (1993).
- [75] F. D. M. Haldane, Nonlinear field theory of large-spin Heisenberg antiferromagnets: Semiclassically quantized solitons of the one-dimensional easy-axis Néel state, *Phys. Rev. Lett.* **50**, 1153 (1983).
- [76] I. Affleck, T. Kennedy, E. H. Lieb, and H. Tasaki, Rigorous results on valence-bond ground states in antiferromagnets, *Phys. Rev. Lett.* **59**, 799 (1987).
- [77] I. Peschel, X. Wang, M. Kaulke, and K. Hallberg, *Density-Matrix Renormalization - A New Numerical Method in Physics*, 2nd ed. (Springer Berlin, Heidelberg, 1999).
- [78] Z.-C. Gu and X.-G. Wen, Tensor-entanglement-filtering renormalization approach and symmetry-protected topological order, *Phys. Rev. B* **80**, 155131 (2009).
- [79] A. V. Chubukov, S. Sachdev, and J. Ye, Theory of two-dimensional quantum Heisenberg antiferromagnets with a nearly critical ground state, *Phys. Rev. B* **49**, 11919 (1994).
- [80] R. Coldea, D. A. Tennant, E. M. Wheeler, E. Wawrzynska, D. Prabhakaran, M. Telling, K. Habicht, P. Smeibidl, and K. Kiefer, Quantum criticality in an Ising chain: Experimental evidence for emergent E_8 symmetry, *Science* **327**, 177 (2010).
- [81] Z. Wang, T. Lorenz, D. I. Gorbunov, P. T. Cong, Y. Kohama, S. Niesen, O. Breunig, J. Engelmayer, A. Herman, J. Wu, K. Kindo, J. Wosnitza, S. Zherlitsyn, and A. Loidl, Quantum criticality of an Ising-like spin-1/2 antiferromagnetic chain in a transverse magnetic field, *Phys. Rev. Lett.* **120**, 207205 (2018).
- [82] M. Fava, R. Coldea, and S. A. Parameswaran, Glide symmetry breaking and ising criticality in the quasi-1d magnet CoNb_2O_6 , *PNAS* **117**, 25219 (2020).
- [83] C. M. Morris, N. Desai, J. Viirik, D. Hüvonen, U. Nagel, T. Rööm, J. W. Krizan, R. J. Cava, T. M. McQueen, S. M. Koohpayeh, R. K. Kaul, and N. P. Armitage, Duality and domain wall dynamics in a twisted Kitaev chain, *Nature Physics* **17**, 832 (2021).
- [84] J. A. Kjäll, F. Pollmann, and J. E. Moore, Bound states and E_8 symmetry effects in perturbed quantum Ising chains, *Phys. Rev. B* **83**, 020407 (2011).
- [85] T. Liang, S. M. Koohpayeh, J. W. Krizan, T. M. McQueen, R. J. Cava, and N. P. Ong, Heat capacity peak at the quantum critical point of the transverse Ising magnet CoNb_2O_6 , *Nat. Commun.* **6**, 7611 (2015).
- [86] Y. Xu, L. S. Wang, Y. Y. Huang, J. M. Ni, C. C. Zhao, Y. F. Dai, B. Y. Pan, X. C. Hong, P. Chauhan, S. M. Koohpayeh, N. P. Armitage, and S. Y. Li, Quantum critical magnetic excitations in spin-1/2 and spin-1 chain systems, *Phys. Rev. X* **12**, 021020 (2022).
- [87] L. Woodland, D. Macdougall, I. M. Cabrera, J. D. Thompson, D. Prabhakaran, R. I. Bewley, and R. Coldea, Tuning the confinement potential between spinons in the ising chain compound CoNb_2O_6 using longitudinal fields and quantitative determination of the microscopic hamiltonian, *Phys. Rev. B* **108**, 184416 (2023).
- [88] Y. Cui, J. Dai, P. Zhou, P. S. Wang, T. R. Li, W. H. Song, J. C. Wang, L. Ma, Z. Zhang, S. Y. Li, G. M. Luke, B. Normand, T. Xiang, and W. Yu, Mermin-Wagner physics, (H, T) phase diagram, and candidate quantum spin-liquid phase in the spin- $\frac{1}{2}$ triangular-lattice antiferromagnet $\text{Ba}_8\text{CoNb}_6\text{O}_{24}$, *Phys. Rev. Mater.* **2**, 044403 (2018).
- [89] A. V. Chubukov, T. Senthil, and S. Sachdev, Universal magnetic properties of frustrated quantum antiferromagnets in two dimensions, *Phys. Rev. Lett.* **72**, 2089 (1994).
- [90] A. V. Chubukov and D. I. Golosov, Quantum theory of an antiferromagnet on a triangular lattice in a magnetic field, *J. Phys.: Condens. Matter* **3**, 69 (1991).

- [91] O. A. Starykh, Unusual ordered phases of highly frustrated magnets: a review, *Rep. Prog. Phys.* **78**, 052502 (2015).
- [92] B. Bernu, C. Lhuillier, and L. Pierre, Signature of Néel order in exact spectra of quantum antiferromagnets on finite lattices, *Phys. Rev. Lett.* **69**, 2590 (1992).
- [93] L. Capriotti, A. E. Trumper, and S. Sorella, Long-range Néel order in the triangular Heisenberg model, *Phys. Rev. Lett.* **82**, 3899 (1999).
- [94] S. R. White and A. L. Chernyshev, Néel order in square and triangular lattice Heisenberg models, *Phys. Rev. Lett.* **99**, 127004 (2007).
- [95] N. Elstner, R. R. P. Singh, and A. P. Young, Finite temperature properties of the spin-1/2 Heisenberg antiferromagnet on the triangular lattice, *Phys. Rev. Lett.* **71**, 1629 (1993).
- [96] S. A. Kulagin, N. Prokof'ev, O. A. Starykh, B. Svistunov, and C. N. Varney, Bold diagrammatic monte carlo method applied to fermionized frustrated spins, *Phys. Rev. Lett.* **110**, 070601 (2013).
- [97] Y. Doi, Y. Hinatsu, and K. Ohoyama, Structural and magnetic properties of pseudo-two-dimensional triangular antiferromagnets $\text{Ba}_3\text{MSb}_2\text{O}_9$ ($M = \text{Mn, Co, and Ni}$), *J. Phys.: Condens. Matter* **16**, 8923 (2004).
- [98] H. D. Zhou, C. Xu, A. M. Hallas, H. J. Silverstein, C. R. Wiebe, I. Umegaki, J. Q. Yan, T. P. Murphy, J.-H. Park, Y. Qiu, J. R. D. Copley, J. S. Gardner, and Y. Takano, Successive phase transitions and extended spin-excitation continuum in the $S = \frac{1}{2}$ triangular-lattice antiferromagnet $\text{Ba}_3\text{CoSb}_2\text{O}_9$, *Phys. Rev. Lett.* **109**, 267206 (2012).
- [99] T. Susuki, N. Kurita, T. Tanaka, H. Nojiri, A. Matsuo, K. Kindo, and H. Tanaka, Magnetization process and collective excitations in the $S = 1/2$ triangular-lattice Heisenberg antiferromagnet $\text{Ba}_3\text{CoSb}_2\text{O}_9$, *Phys. Rev. Lett.* **110**, 267201 (2013).
- [100] J. Ma, Y. Kamiya, T. Hong, H. B. Cao, G. Ehlers, W. Tian, C. D. Batista, Z. L. Dun, H. D. Zhou, and M. Matsuda, Static and dynamical properties of the spin-1/2 equilateral triangular-lattice antiferromagnet $\text{Ba}_3\text{CoSb}_2\text{O}_9$, *Phys. Rev. Lett.* **116**, 087201 (2016).
- [101] S. Ito, N. Kurita, H. Tanaka, S. Ohira-Kawamura, K. Nakajima, S. Itoh, K. Kuwahara, and K. Kakurai, Structure of the magnetic excitations in the spin-1/2 triangular-lattice Heisenberg antiferromagnet $\text{Ba}_3\text{CoSb}_2\text{O}_9$, *Nature Commun.* **8**, 235 (2017).
- [102] R. Rawl, L. Ge, H. Agrawal, Y. Kamiya, C. R. Dela Cruz, N. P. Butch, X. F. Sun, M. Lee, E. S. Choi, J. Oitmaa, C. D. Batista, M. Mourigal, H. D. Zhou, and J. Ma, $\text{Ba}_8\text{CoNb}_6\text{O}_{24}$: A spin- $\frac{1}{2}$ triangular-lattice Heisenberg antiferromagnet in the two-dimensional limit, *Phys. Rev. B* **95**, 060412 (2017).
- [103] M. M. Bordelon, E. Kenney, C. Liu, T. Hogan, L. Posthuma, M. Kavand, Y. Lyu, M. Sherwin, N. P. Butch, C. Brown, M. J. Graf, L. Balents, and S. D. Wilson, Field-tunable quantum disordered ground state in the triangular-lattice antiferromagnet NaYbO_2 , *Nature Physics* **15**, 1058 (2019).
- [104] K. M. Ranjith, D. Dmytriieva, S. Khim, J. Sichelschmidt, S. Luther, D. Ehlers, H. Yasuoka, J. Wosnitza, A. A. Tsirlin, H. Kühne, and M. Baenitz, Field-induced instability of the quantum spin liquid ground state in the $J_{\text{eff}} = \frac{1}{2}$ triangular-lattice compound NaYbO_2 , *Phys. Rev. B* **99**, 180401 (2019).
- [105] Z. Zhu and S. R. White, Spin liquid phase of the $s = \frac{1}{2} J_1 - J_2$ heisenberg model on the triangular lattice, *Phys. Rev. B* **92**, 041105 (2015).
- [106] W.-J. Hu, S.-S. Gong, W. Zhu, and D. N. Sheng, Competing spin-liquid states in the spin- $\frac{1}{2}$ heisenberg model on the triangular lattice, *Phys. Rev. B* **92**, 140403 (2015).
- [107] Y. Iqbal, W.-J. Hu, R. Thomale, D. Poilblanc, and F. Becca, Spin liquid nature in the heisenberg $J_1 - J_2$ triangular antiferromagnet, *Phys. Rev. B* **93**, 144411 (2016).
- [108] S. Hu, W. Zhu, S. Eggert, and Y.-C. He, Dirac spin liquid on the spin-1/2 triangular heisenberg antiferromagnet, *Phys. Rev. Lett.* **123**, 207203 (2019).
- [109] T. Itou, A. Oyamada, S. Maegawa, and R. Kato, Instability of a quantum spin liquid in an organic triangular-lattice antiferromagnet, *Nature Physics* **6**, 673 (2010).
- [110] N. E. Sherman, M. Dupont, and J. E. Moore, Spectral function of the $J_1 - J_2$ heisenberg model on the triangular lattice, *Phys. Rev. B* **107**, 165146 (2023).
- [111] P. Czarnik, J. Dziarmaga, and P. Corboz, Time evolution of an infinite projected entangled pair state: An efficient algorithm, *Phys. Rev. B* **99**, 035115 (2019).
- [112] J. Haegeman, C. Lubich, I. Oseledets, B. Vandereycken, and F. Verstraete, Unifying time evolution and optimization with matrix product states, *Phys. Rev. B* **94**, 165116 (2016).
- [113] J. Haegeman, M. Mariën, T. J. Osborne, and F. Verstraete, Geometry of matrix product states: Metric, parallel transport, and curvature, *J. Math. Phys.* **55**, 021902 (2014).
- [114] M.-D. Choi, Positive linear maps on c^* -algebras, *Canadian Journal of Mathematics* **24**, 520 (1972).